1 # A method for improving hotspot directional signatures in BRDF models used for

2 # MODIS

3

4 Ziti Jiao[1,2,*], Crystal B. Schaaf [3,4], Yadong Dong[1,2], Miguel Román[5],

5 Michael J. Hill[6], Jing M. Chen[7], Zhuosen Wang[3,4,5], Hu Zhang [1,2], Edward Saenz[3],

6 Rajesh Poudyal[8], Charles Gatebe[9], Francois-Marie Bréon[10], Xiaowen Li [1,2], Alan Strahler[4]

7

8 [1] State Key Laboratory of Remote Sensing Science, Research Center for Remote Sensing and GIS, and School of
9 Geography, Beijing Normal University. Beijing 100875, China;
10 [2] Beijing Key Laboratory of Environmental Remote Sensing and Digital City, Beijing Normal University, Beijing 100875,
11 China
12 [3] Department of Environmental, Earth and Ocean Sciences, University of Massachusetts, Boston, MA, USA
13 [4] Center for Remote Sensing, Department of Earth and Environment, Boston University, Boston, MA, USA
14 [5] Terrestrial Information Systems Laboratory, NASA Goddard Space Flight Center, Greenbelt, MD, USA
15 [6] Department of Earth System Science and Policy, University of North Dakota, Clifford hall, 4149 University Avenue,
16 Grand Forks, ND, 58202
17 [7] Department of Geography and Program in Planning, University of Toronto, 100 St. George St., Room 5047, Toronto,
18 Ontario, Canada M5S 3G3
19 [8] Science Systems & Applications, Inc., NASA Goddard Space Flight Center, Lanham, MD, USA
20 [9] Universities Space Research Association, NASA Goddard Space Flight Center, Greenbelt, Maryland, USA
21 [10] Laboratoire des Sciences du Climat et de l'Environnement, CEA/DSM/LSCE, 91191 Gif sur Yvette, France
22 *email: jiaozt@bnu.edu.cn

23

24

Abstract:

The semi-empirical, kernel-driven, linear RossThick-LiSparseReciprocal (RTLSR) Bidirectional Reflectance Distribution Function (BRDF) model is used to generate the routine MODIS BRDF/Albedo product due to its global applicability and the underlying physics. A challenge of this model in regard to surface reflectance anisotropy effects comes from its underestimation of the directional reflectance signatures near the Sun illumination direction; also known as the hotspot effect. In this study, a method has been developed for improving the ability of the RTLSR model to simulate the magnitude and width of the hotspot effect. The method corrects the volumetric scattering component of the RTLSR model using an exponential approximation of a physical hotspot kernel, which recreates the hotspot magnitude and width using two free parameters (C_1 and C_2, respectively). The approach allows one to reconstruct, with reasonable accuracy, the hotspot effect by adjusting or using the prior values of these two hotspot variables. Our results demonstrate that: (1) significant improvements can be made to this method by using the inverted hotspot parameters; (2) the reciprocal nature allow this method to be more adaptive for simulating the hotspot height and width with high accuracy, especially in cases where hotspot signatures are available; and (3) while the new approach is consistent with the heritage RTLSR model inversion used to estimate intrinsic narrowband and broadband albedos, it presents some differences for vegetation clumping index (CI) retrievals. With the hotspot-related model parameters determined *a priori*, this method offers improved performance for various ecological remote sensing applications; including the estimation of canopy structure parameters.

2

47

1. Introduction

Semi-empirical kernel-driven linear Bidirectional Reflectance Distribution Function (BRDF) models have been widely used to determine the properties of complex heterogeneous environments from multi-angle remote sensing. These models have been used to produce the routine BRDF/Albedo products from the Moderate Resolution Imaging Spectroradiometer (MODIS) (Lucht et al., 2000; Schaaf et al., 2002; Schaaf et al., 2011), the Polarization and Directionality of the Earth's Reflectances (POLDER) (Bicheron and Leroy, 2000; Bacour and Bréon, 2005), the Meteosat Second Generation (MSG) (van Leeuwen and Roujean, 2002; Geiger et al., 2005), and the Visible/Infrared Imager/Radiometer Suite (VIIRS) on board the platforms of the Suomi National Polar-orbiting Partnership (NPP) (Justice et al., 2013). They have been also used to retrieve canopy structure parameters (e.g., Chopping et al., 2008; Wang et al., 2011; Hill et al., 2011; He et al., 2012), to examine the improved accuracy of land cover classification (de Colstoun et al., 2006; Jiao, Woodcock & Schaaf et al, 2011; Jiao & Li, 2012), to accumulate and apply prior knowledge of BRDF archetypal shapes (Li, Gao, Wang & Strahler, 2001; Jiao, Hill, Schaaf et al., 2014; Jiao, Zhang & Dong et al., 2015), to couple surface reflectance with atmospheric scattering for improving atmospheric correction algorithms (Hu et al., 1999; Wang et al., 2010; Román et al., 2010; Litvinov et al., 2011), to correct for the effect of remotely-sensed anisotropic reflectance (e.g., Leroy and Roujean, 1994; Li et al., 1996), and for monitoring ecosystem disturbance and vegetation dynamics (e.g., Friedl et al., 2002, 2010; Zhang et al., 2003).

Despite their wide use, recent studies have recognized that the directional signatures near

4

69 the Sun illumination direction (aka the hotspot effect) are often underestimated by the

70 semi-empirical BRDF models (e.g., Chen and Cihlar, 1997; Maignan et al., 2004; Román et al.,

71 2011) such as RTLSR (Wanner et al., 1995; Lucht et al., 2000). In particular, the volumetric

72 scattering (aka Ross) component of RTLSR, originally derived from a horizontally homogeneous

73 plant canopy (Ross, 1981), does not include all possible correlations between the illumination

74 and observation geometries (Kuusk, 1991; Jupp and Strahler, 1991; Qin & Geol, 1995). Although

75 the geometric-optical (Li-Strahler) component derived from geometric optical (GO) models

76 characterizes a significant hotspot effect (Li and Strahler, 1992), the RTLSR model that linearly

77 combines these two (Ross and Li-Strahler) components has difficulties to simulate the both the

78 magnitude and signature of the hotspot effect. This model deficiency, while not significantly

79 impacting an albedo retrieval (Huang, Jiao & Dong et al., 2013) (based on the integral of the

80 entire view-illumination hemisphere), may still constrain the application of BRDF models in

81 retrieving canopy structure parameters (e.g., clumping index) that need the hotspot amplitude as

82 primary input (e.g., He et al., 2012; Zhu et al., 2012).

83   Various efforts have been made to improve the hotspot effect for such models. Chen and

84 Cihlar (1997) enhanced the hotspot effect of the kernel-driven Roujean BRDF model by

85 multiplying the model with an exponential approximation of a physically-based hotspot function.

86 He et al. (2012) and Zhu et al. (2012) suggested that the Chen and Cihlar (1997) model might

87 still slightly underestimate the reflectance magnitude when it is used to extrapolate the hotspot.

88 Recent efforts have focused on correcting the RossThick kernel with a hotspot factor (Maignan

89 & Bréon et al., 2004; hereafter referred to as the Maignan method) based on the geometrical

90   principles of the intersection of viewed and sunlit leaf areas (Jupp and Strahler, 1991). With a

91   view to improving retrieval of clumping index (CI) from the MODIS BRDF product, He at al.

92   (2012) also developed a correction for the MODIS hotspot amplitude by adding the difference

93   between POLDER and MODIS hotspot BRFs, which has also been used to correct the hotspot

94   magnitude of MISR BRFs for CI retrievals (Pisek, Ryu, Sprintsin & He et al., 2013). On the

95   other hand, Zhu et al. (2012) corrected the hotspot amplitude by multiplying both the geometric

96   optical scattering and volumetric scattering items by the exponential approximation of a

97   modified hotspot function; also based on the MODIS RTLSR model.

98   In this study, we propose a method for improving the hotspot effect of the linear RTLSR

99   BRDF model. The method revises the RossThick kernel using the corrected exponential

100   approximation of the hotspot function (Chen and Cihlar, 1997, thereafter named RTCLSR model

101   here). The principle of the formation of the hotspot is based on a canopy gap size distribution

102   function, but is approximated by using an exponential function with two free parameters (C_1 and

103   C_2) characterizing the height and width of the hotspot effect. The hotspot kernel within-crown

104   and between-crown has very similar shapes, and thus can be directly applied to the scenario

105   where a canopy cover is provided with a uniform leaf orientation of horizontally homogeneous

106   plant canopies, as was used in the assumption in deriving this kernel from canopy radiative

107   transfer theory (Ross, 1981). Such a correction to the RossThick kernel mainly accounts for the

108   correlation between two gap probabilities from sun and view in the hotspot direction, which was

109   not properly considered when deriving the original RossThick kernel.

110   To validate this model, the study uses a variety of hotspot data to determine appropriate

6

hotspot-related parameters including POLDER, MODIS, airborne multiangle Cloud Absorption

Radiometer (CAR) (King et al., 1986, Gatebe et al., 2003, Román et al., 2011), and two

field-measured data sets (Irons et al., 1992; Deering et al., 1999). We also explore the sensitivity

of two hotspot parameters (C_1 and C_2) to hotspot-fits. Finally, we examined the influences of this

new approach on the retrieval of intrinsic albedos and clumping index.

2. Hotspot data

2.1. POLDER-3 BRDF database

The spaceborne POLDER instrument can sample the land surface for viewing angles up to

60°-70° and for the full azimuth range, at a coarse spatial resolution of approximately 6 km.

Comprehensive BRDF sampling with large spatial coverage enables this instrument to collect

observations for the development of BRDF modeling, particularly capturing distinct hotspot

signatures. The POLDER-3 sensor onboard the Polarization and Anisotropy of Reflectances for

Atmospheric Sciences coupled with Observations from a Lidar (PARASOL) satellite acquired

multiangular measurements for more than 6 years, which were used to create four BRDF

databases (Bréon et al., 2007). The approach uses POLDER data from relatively homogeneous

pixels to represent the dominant continental ecosystems. The data are geocoded, calibrated,

atmospherically-corrected and cloudy-screened for acquiring the land surface bidirectional

reflectance factors (BRFs) for each orbit. This study uses a monthly database containing 14,649

BRFs in 16 IGBP land cover classes. According to phase angle $\xi \leq 5°$, we extract ~14,188 BRFs.

The spatial distribution of view and Sun geometries for a typical POLDER data set, i.e.,

IGBP_01_20060609brdf_ndvi08.0824_1671, is exemplified in Figure 1 (b). Since the 'Snow and

Ice' class tends to have maximum reflectance in forward scattering direction that current surface

BRF models cannot characterize, we exclude this class from the database. The BRDF signatures

are based on inversions of approximately 20 orbits worth of spectral BRF data, for each of the

six POLDER bands. Up to 16 different multiangular measurements for a given POLDER pixel

are included in each orbit. BRFs measured at two typical bands (red, centered 670 nm and NIR,

centered 865 nm) are mainly selected to assess the hotspot effect reconstructed from the

proposed model. Notably, POLDER-3 spectral measurements are not simultaneous, meaning that

each channel is acquired with a slightly different viewing geometry. As such, to analyze the

variability of hotspot signatures, this requires a careful assessment of measurement differences,

including normalization of the POLDER viewing geometry (Bréon et al., 2005).

2.2. MODIS hotspot data

We extracted 2,275 MODIS hotspot data sets from one $10° \times 10°$ tile (h20v11) of MODIS

surface reflectance products (MOD09 and MYD09) at a spatial resolution of approximately

500-m, for 7 solar reflective bands, and using high-quality BRDF sampling distributions,

represented by a phase angle range $\xi \leq 5°$. There are only 80 high-quality hotspot data sets within

a phase angle range of $\xi \leq 1.5°$; indicating that MODIS seldom acquires exact hotspot

observations. Each data set consists of at least 10 observations with a proper directional sampling

in approximate principal plane (PP), and includes fewer hotspot measurements within the

defined area (Figure 1, a). The corresponding MODIS tile h20v11 captures a wide range of

grass-shrub-savanna vegetation types in the Southern Hemisphere. The 329th Day of Year (DOY)

in 2010 represents a maturity season (Zhang et al., 2003). Solar zenith angles (SZAs) mainly

153 ranged from 20° to 40° during the study period. The full-model inversion quality of the MODIS

154 BRDF/Albedo product (MCD43A2) accounts for approximately 70 % of total pixels. The spatial

155 distribution of MODIS observations and solar geometry from an extreme data set in this tile is

156 presented in Figure 1 (c), where solid points are for MODIS observations, and circles are for

157 solar geometries. The concentric circles are at 20° intervals.

158 Since the Terra and Aqua MODIS accumulate multiangular observations through multiple

159 overlapping image swaths, the solar geometry corresponding to each observation will be

160 different during a typical (16-day) retrieval period (e.g., approximately 20° for SZA in the

161 h20v11 tile). This means that MODIS does not capture enough real-time observations in the

162 principal plane (PP) under identical solar illumination conditions. Here, we adopt the assumption

163 used with the MODIS BRDF/Albedo product, whereby the surface BRDF shape doesn't change

164 abruptly for the range of SZAs capturing during a 16-day retrieval period. With this assumption,

165 we can accumulate some multiangular observations in the proximity of the hotspot (i.e., $\xi \leq 5°$)

166 to constrain the RTCLSR model for acquiring the optimal free parameters describing the hotpot

167 magnitude (C_1) and width (C_2). Figure 1 (d) presents an extreme example that uses the RTCLSR

168 model to reconstruct BRDF shapes as a function of phase angle for IGBP savanna in the NIR

169 band. Red solid points represent observations extracted by using this method in the approximate

170 PP. The black curve is the reconstructed BRDF shape using the RTCLSR model with C_1=0.4,

171 and C_2=4.5° as the optimal values for the 2,275 MODIS data sets in this tile. The SZA was set to

172 30.58°, and the observation in the closest proximity to the hotspot direction is 31° (red point).

173 The BRDF shape reconstructed using the Maignan method (green curve) is provided here for

174 visual comparison.

175   Figure 1 near here

176 **2.3. Finer resolution measurements**

177   We used airborne datasets collected by NASA's Cloud Absorption Radiometer (CAR)

178 (Gatebe et al., 2003), which captures hotspot signatures over 2 field sites. To acquire

179 multiangular measurements, the CAR instrument is flown using a clockwise circular pattern

180 above the surface repeatedly, and observes the reflected solar radiation at a fine angular

181 resolution (i.e., 0.5° intervals through its 190° aperture at a rate of 100 scans per minute). This

182 sampling scheme results in a BRDF retrieval that is based on 76,400 and 114,600 BRFs

183 measurements per channel per complete orbit, which corresponds to a representative sample of

184 the landscape-level (~5 km) reflected surface (Gatebe et al., 2003). At an altitude of 600m above

185 the targeted surface area and 1° instantaneous field of view (IFOV), the pixel resolution is about

186 10 m at nadir and about 270 m at an 80° viewing angle (Tsay et a., 1998). The geolocation

187 accuracy of CAR measurements is within an error margin of 0.3% (~2.0-3.5 meters as derived

188 from the high resolution scene across the entire scan track). This accuracy holds well particularly

189 with off-nadir looking observations (Gatebe et al., 2007). These CAR measurements used in this

190 study are averaged at an angular resolution of 1° in the viewing hemisphere and are taken in the

191 red (0.682 µm) and NIR (0.870 µm) bands.

192   CAR data source was mainly from the early Smoke Clouds and Radiation-Brazil (SCAR-B)

193 field campaign on August, 1995. Two kinds of data sets were collected from the well-defined

194 surfaces of cerrado and dense forest (Tsay et al., 1998), both measured in Brazil under nearly

195 clear-sky conditions (http://car.gsfc.nasa.gov/data/index.php?mis_id=5&n=SCAR-B&l=h). The

196 cerrado comprises a landscape-scale mosaic of four main vegetation types ranging from *campo*

197 *limpo* grassland, through *campo sujo* and *campo ralo* with small (< 2m) sparse-to-medium

198 density woody plants overlaying grassland, to *cerrado sensu str*icto with 20 – 30 t/ha of woody

199 biomass. The dense forest data includes two flight data (i.e., CAR Flight #1689 and CAR Flight

200 #1693). These two forest data captured distinct hotspot signatures in the red (CAR Flight #1689)

201 and the NIR (CAR Flight #1693) bands, and are used in this study. The area of dense forest was

202 covered by tall trees with a large canopy where the ground surface is invisible and had a

203 relatively homogeneous surface. Details about these airborne CAR measurements are referred to

204 Tsay et al. (1998).

205 To compare these models being explored at a field scale, we also analyzed two high-quality

206 multiangular field data sets reported in previous studies (e.g. Li et al., 2001; Strugnell et al., 2001;

207 Huang & Jiao 2012; Jiao et al., 2014). These include soil multiangular measurements (Iron et al.,

208 1992) acquired on a bare field located on a level alluvial plane within the United States

209 Department of Agriculture Beltsville Agricultural Research Center, Beltsville, MD. The data

210 were taken from full view angles and several solar illumination directions. A calibrated Barnes

211 Model 12-1000 Modular Multiband Radiometer (MMR) with a 15° IFOV was used. Forest

212 multiangular measurements (Deering et al., 1999) were also acquired with PARABOLA

213 instrument with a 15° IFOV at a black spruce site that was mainly made up of old black spruce

214 (*picea mariana*) with scattered emergent tamarack. The tree height was less than 10 m and the

215 total stem density was 8040 live stems/ha, with a basal area of 40 m^2/ha. Canopy closure

216 averaged about 55 %, and the leaf area index (LAI) measured by an LAI-2000 in spring 1994

217 was 3.7 (Chen et al., 1997).

3. Model and method

3.1. RTLSR model

220 The semi-empirical, kernel-driven, linear BRDF model is a linear combination of three

221 basic scattering components: isotropic scattering, volumetric scattering, and geometric-optical

222 (GO) scattering. This model adopted a general form (Roujean et al., 1992; Lucht et al., 2000):

223 $$R(\theta_v, \theta_s, \Delta\phi, \lambda) = f_{iso}(\lambda) + f_{vol}(\lambda)K_{vol}(\theta_v, \theta_s, \Delta\phi) + f_{geo}(\lambda)K_{geo}(\theta_v, \theta_s, \Delta\phi) \qquad (1)$$

224 Where $f_{iso}(\lambda)$, $f_{vol}(\lambda)$ and $f_{geo}(\lambda)$ are the spectrally dependent model parameters. $K_{vol}(\theta_v,\theta_s,\Delta\phi)$ and

225 $K_{geo}(\theta_v,\theta_s,\Delta\phi)$ are kernel functions of view zenith θ_v, illumination zenith θ_s and relative azimuth

226 $\Delta\phi$ and provide shapes for volumetric scattering and geometric-optical scattering BRDFs; $f_{iso}(\lambda)$

227 is a spectral constant for isotropic scattering; $f_{vol}(\lambda)$ and $f_{geo}(\lambda)$ are spectral constants, i.e., model

228 anisotropic parameters that weight the two BRDFs; $R(\theta_v,\theta_s,\Delta\phi,\lambda)$ is BRDF in waveband λ.

229 K_{geo} and K_{vol} have been derived from physical approximation of the radiative transfer at the

230 surface. K_{geo} is derived from the GO model (Li and Strahler, 1992; Roujean et al., 1992) and

231 characterizes dome-shaped BRDF curves. It is a function that describes the shadowing and

232 surface scattering from the canopy. The operational MODIS BRDF/Albedo algorithm adopted

233 the LiSparseReciprocal kernel (K_{LSR}) that was derived from a sparsely-vegetated canopy surface.

234 $$K_{LSR} = O(\theta_v, \theta_s, \Delta\phi) - \sec\theta_v' - \sec\theta_s' + \frac{1}{2}(1 + \cos\xi')\sec\theta_v' \sec\theta_s' \qquad (2)$$

235 Notably, where $O(\theta_v,\theta_s,\Delta\phi)$ is overlap function of view and illumination shadows on the ground,

236 and hence the hotspot effect (i.e., the probability of seeing the sunlit background from the same

237 gap) is included in this kernel. Further expressions and several intermediate variables are detailed

238 to several papers (e.g., Wanner et al., 1995; Lucht et al., 2000).

239 Notably, two ratios (h/b and b/r) for describing vegetation structure are used to parameterize

240 overlap function in K_{LSR}. Here, h is the mean height where a crown center is located, b is the

241 mean vertical half axis of the modeled ellipsoid, and r is the mean horizontal radius. These two

242 ratios are related to the hotspot effects in K_{LSR} on vegetation canopy scale (Li and Strahler, 1992).

243 The operational MODIS RTLSR algorithm adopts h/b=2 and b/r=1. In Figure 2 (top), red dashed

244 curve is for h/b=2 and b/r=1.2, and magenta dashed curve is for h/b=2.5 and b/r=1. Figure 2

245 demonstrates that, although these two ratios were in theory related to the general hotspot effect in

246 K_{LSR}, they do not seem to be very sensitive to the changes of hotspot effect at a reasonable range.

247 K_{vol} is a similar function that describes the volumetric scattering component from canopy,

248 based on an assumption of a single-scattering approximation of the radiative transfer (RT) theory

249 by Ross (1981). The operational RTLSR model adopted RossThick kernel (K_{RT}) derived from a

250 homogenously layered canopy with a large leaf area index (LAI) (Wanner et al., 1995)

251 $$K_{RT} = \frac{\left(\frac{\pi}{2} - \xi\right)\cos\xi + \sin\xi}{\cos\theta_v + \cos\theta_s} - \frac{\pi}{4} \tag{3}$$

252 This kernel characterizes bowl-shaped BRDF curves, but does not consider the correlation

253 between illumination and observation processes for the observed hotspot. In theory, the

254 probability of observing a sunlit component can be taken as the product of two probabilities: one

13

255   for the view line from the observer and the other for illumination beam from Sun. When the view

256   line and an illumination beam coincide, the observer either sees the sunlit foliage or the sunlit

257   background, while the shadows of foliage and background are hidden from the view. As a result,

258   the correlation tends to be 1:1, as the illumination and view directions get closer.

259   **3.2. RTLSR hotspot correction**

260   To consider the correlation between the view and illumination processes, Maignan et al.

261   (2004) corrected the K_{RT} with a hotspot factor:

262    $$K_{RTM} = \frac{\left(\frac{\pi}{2} - \xi\right)\cos \xi + \sin \xi}{\cos \theta_v + \cos \theta_s} \times \left(1 + \left(1 + \xi / \xi_0\right)^{-1}\right) - \frac{\pi}{4} \qquad (4)$$

263    $1 + \left(1 + \xi / \xi_0\right)^{-1}$ is a simplified hotspot factor derived by Bréon et al. (2002) from the theory on

264   the calculation of an overlay function of the intersection of viewed and sunlit leaf areas (Jupp &

265   Strahler, 1991). This hotspot factor was used to correct K_{RT}, thereafter named K_{RTM}. Here ξ is

266   phase angle, ξ_0 is a characteristic angle in relation to the ratio of scattering element size and the

267   canopy vertical density, which follows the range $\xi_0 = [1°, 2°]$. A $\xi_0 = 1.5°$ has been suggested as a

268   typical value representing a wide range of landscape conditions (Bréon et al., 2002; Maignan et

269   al., 2004).

270   Note that the K_{RTM} value near the hotspot direction will double rapidly (as much as K_{RT}) as

271   the phase angle ξ approaches 0°. To consider hotspot variability, we specified a $\xi_0 = 3.0°$ for

272   K_{RTM} for a comparison with the standard $\xi_0 = 1.5°$ (Figure 2). The results indicate that an increase

273   in ξ_0 can increase hotspot width, but diverge from K_{RT} beyond the hotspot region compared

274   with K_{RTC}. Therefore, we do not further examine the ξ_0 influence on hotspot-fits in this study,

275   rather than adopt $\xi_0 = 1.5°$ as the most appropriate value. Here, the K_{RTM} has a simplified feature

276   whereby the variation in hotspot height and width is determined by phase angle ξ.

277   For volumetric scattering kernel (K_{vol}), it is frequently required to meet the empirical

278   requirement of $K_{vol} = 0$ when both the viewing and illumination geometries point to nadir. This

279   requirement aims to ensure that the isotropic parameter is physically reflectance for the model

280   retrieval (Roujean et al., 1992). Conversely, using the Maignan method, the nadir-view and

281   nadir-sun reflectance are specified as $R(0,0,0,\lambda) = f_{iso}(\lambda) + f_{vol}(\lambda) \times \pi/4$.

282   Here, we introduce the modified exponential function of the hotspot kernel function to K_{RT},

283   hereby termed the RossThickChen kernel (K_{RTC}), which includes two free parameters

284   characterizing hotspot variations (Chen and Cihlar, 1997):

285
$$K_{RTC} = \frac{\left(\frac{\pi}{2} - \xi\right)\cos\xi + \sin\xi}{\cos\theta_v + \cos\theta_s} \times \left(1 + C_1 e^{-\frac{\xi}{C_2}}\right) - \frac{\pi}{2} \tag{5}$$

286   Where $1 + C_1 e^{-\frac{\xi}{C_2}}$ is the modified hotspot function. The two free parameters, C_1 and C_2, allow a

287   large dynamic range of hotspot variation, and thus facilitate the analysis of the variation of

288   hotspot height and width in fitting hotspot BRFs. For this retrieval, we also make an empirical

289   adjustment to retain the isotropic BRDF model parameter, f_{iso}, as the corresponding nadir-view

290   and nadir-sun BRF.

291   Originally, the K_{RTC} hotspot function was derived from a theoretical expression that

292   accounts for the hotspot effect for a forest stand, based on a geometric-optical model (Chen &

293   Leblanc, 1997). In this specific scenario, C_1, is linearly related to the difference between the

294   reflectances of the foliage and background at the wavelengths of interest (Chen & Cihlar, 1997).

295   In deriving this hotspot kernel, Chen and Leblanc (1997) demonstrated that this modification had

296   very similar shapes at within-crown and between-crown scales because the gap size is scaled by

297   the gap depth. For plane parallel layers of leaves, the average gap depth is taken as the mean

298   distance between two layers of leaves and is related to the leaf area density. In this hotspot

299   function (K_{RTC}), C_1 is related to the magnitude of the hotspot peak, while C_2 defines the half

300   width of the hotspot in relation to the ratio of canopy height to the size of the predominant

301   canopy structure. Notably for this study, to keep consistent with the original kernel form, the unit

302   of C_2 is radians in terms of Eq. (5), but it is converted into degrees in subsequent use to describe

303   the hotspot width.

304   Here, the K_{RTC} kernel is empirically adjusted to meet $K_{RTC} = 0$ for the nadir-view and

305   nadir-sun geometries, which results in a downward shift of kernel shape (Figure 2, bottom). Note

306   that this adjustment does not affect the fitting ability of this model since the kernel shape is

307   retained. Figure 2 aligns K_{RTC} with K_{RT} and K_{RTM} for a convenient comparison. The results

308   indicate that K_{RTC} coincides with K_{RT} in the scattering direction beyond hotspot region, and

309   adjusts the hotspot height and width by changing C_1 and C_2 (Figure 2 bottom). A larger C_1 value

310   also indicates a higher hotspot, while a larger C_2 value indicates a wider hotspot.

311   Figure 2 near here

312   **3.3. Hotspot parameter retrieval and analysis**

313   The inversion strategy for retrieving the three parameters of this linear BRDF model is to

314   minimize the root mean square error (RMSE) between model predicted and observed BRFs. The

16

315 full-inversion is a simple matrix inversion that is independent of land surface types and is

316 performed pixel by pixel using all high-quality measurements available. Details are referred to

317 the papers (Roujean et al., 1992; Lucht et al., 2000; Shuai et al, 2008).

318   To derive the C_1 and C_2 values, we calculated fit-RMSEs to minimize the

319 model-observation fits using accumulated measurements in a close vicinity to the hotspot

320 direction (i.e., $\xi \leq 5°$).

321 $$RMSE = \sqrt{\frac{\sum_{j=1}^{n}\left(R^{obs}(\theta_v,\theta_s,\Delta\phi,\lambda) - R^{model}(\theta_v,\theta_s,\Delta\phi,\lambda)\right)^2}{n-3}}$$ (6)

322 Where R^{obs} $(\theta_v,\theta_s,\Delta\phi,\lambda)$ and R^{model} $(\theta_v,\theta_s,\Delta\phi,\lambda)$ are the model predicted and observed BRFs near

323 the hotspot region in the viewing and solar geometries, θ_v, θ_s, $\Delta\phi$ at wavelength λ, as in Equation

324 (1). We derived the optimized C_1 and C_2 values from the least RMSEs using the iteration step

325 size of 0.1 for $C_1 = [0.3,1.2]$ and $C_2 = [1.0°,6.0°]$. This range of C_1 and C_2 can ensure realistic

326 hotspot variations while optimizing processing time. Following this method, we retrieved the C_1

327 and C_2 values for the entire POLDER database; including parameterizations by IGBP cover type

328 and phenological phase, respectively. To derive the optimal hotspot parameter values, we

329 constrain this model by accumulating all measurements near hotspot direction ($\xi \leq 5°$) for these

330 two parameter types, including all 15 IGBP classes, excluding 'Snow and Ice' and 2 phenological

331 stages: (1) maturity and (2) dormancy.

332   We then compared the model predicted and observed BRFs near hotspot direction by using

333 scatterplots with regression lines. To display model-observation fits, we examined the model

334 predicted and observed BRFs as a function of phase angle for the selected observations for

335　Evergreen Needleleaf Forest type (ENF) for each of POLDER's reflective bands. Details on how

336　to derive the shaded area (Figure 1, a) are provided in Appendix A. We also performed a

337　comparison against finer resolution in-situ data. To analyze the sensitivity of the hotspot

338　parameters to hotspot-fits in conjunction with the model parameters, we used simulated BRDF

339　shapes generated from the airborne CAR data set.

340　　Finally, we examined the intrinsic albedos (i.e., White Sky Albedo (WSA) and Black Sky

341　Albedo (BSA)) and clumping index (CI) retrievals between models. To retrieve CI values, we

342　made use of the algorithm by Chen et al. (2005) and assigned a simplified geometry of 45° view

343　zenith angles in both the backward- and forward- scattering directions for the corresponding

344　principal plane hotspot and dark spot, respectively (Zhu et al. 2012). Such a simplification is

345　somewhat different from Chen et al. (2005), which focused on locating the optimal view

346　geometry to capture the dark spot. Since the three models are generally consistent in fitting

347　observations outside of the hotspot region, this simplification would not affect the

348　inter-comparison of CI retrievals between models.

349　**4. Results**

350　**4.1. C_1 and C_2 values for POLDER**

351　　In this section, we assess the performance of the two hotspot parameters, based on the

352　underlying IGBP class and two vegetation phenological phases, based on a comparison of the

353　model predicted hotspot BRFs with observed BRFs derived from the POLDER BRDF database.

354　For this study, our analysis focuses on the RTCLSR and Maignan method.

4.1.1. Hotspot parameters in regard to surface type and phenology

Figure 3 (top left) presents the globally optimized C_1 and C_2 values (RTCLSR_GLOB) for 6 POLDER bands [490, 565, 670, 765, 865, and 1020nm]. These values indicate the variation trend of hotspot parameters for the available POLDER BRDF database. In general, the spectral variations of C_1 and C_2 present a highly negative correlation ($R^2 = 0.58$). This indicates that a higher hotspot magnitude also tends to go with a narrower shaped hotspot, and vice versa. Figure 3 (middle) presents the optimized C_1 and C_2 values derived for underlying IGBP classes in the red and NIR bands. Results indicate that the C_1 values in the red band are larger than in the NIR for all IGBP classes; indicating that the hotspot height is relatively prominent in red band. This is due to the higher-level chlorophyll absorption of vegetation foliage in the red band, which strengthens the sunlit-shaded component contrast, and results in a more prominent reflectance anisotropy. The C_1 values are significantly different between some IGBP classes; particularly in the red, and exhibits a high correlation between the red and the NIR ($R^2 = 0.62$). This reveals that a higher hotspot in the red band is frequently accompanied by a higher hotspot in the NIR band. However, the C_2 parameter presents a low correlation between the two bands ($R^2 = 0.21$), indicating that hotspot width is not band-dependent for these BRDF data.

Figure 3 (top right) shows the near-hotspot fit-RMSEs ($\xi < 5°$) between models in 6 bands. Results indicate that the fit-RMSEs are lower in the visible than in NIR and shortwave infrared (SWIR). As expected, the RTLSR model had the largest fit-RMSEs in the vicinity of hotspot direction. We also derived globally optimized fit-RMSEs (RTCLSR_GLOB) for the entire POLDER data and the IGBP-bounded fit-RMSEs (RTCLSR_IGBP). The absolute average

19

376 difference (AAD) of the fit-RMSEs (left ordinate) between Maignan and RTCLSR_IGBP models

377 was 0.0023 per band, while the relative average difference (RAD) of fit-RMSEs (right ordinate)

378 between these two models was ~20-30% in the blue, red and NIR bands [490, 670, 765nm]. This

379 reveals that the RTCLSR model with the two free parameters can provide further improved

380 hotspot-fits. Figure 3 (bottom) presents the fit-RMSEs for 15 IGBP classes between models in

381 the red and NIR bands. Some improvements occur for several IGBP classes using the RTCLSR.

382 The improvements seem more pronounced for forest than for herbaceous classes in the red band,

383 while the opposite appeared to be the case in the NIR band.

384   Figure 3 near here

385   To examine the phenological response of C_1 and C_2 values for surface type, we used

386 mid-high latitude ($23.5° \leq$ latitude $\leq 60°$) POLDER data in terms of the timing of Jun-Jul-Aug

387 and Dec-Jan-Feb in Northern Hemisphere to represent maturity and dormancy seasons; using

388 opposite time periods in the Southern Hemisphere. The C_1 and C_2 values were then retrieved for

389 each IGBP class in the red and NIR bands. Figure 4 shows that vegetation cover tends to have

390 larger C_1 and C_2 values in maturity, but less C_1 and C_2 values in dormancy in the red band. In the

391 NIR band, vegetation cover mainly captures less C_1 but larger C_2 in maturity and larger C_1 but

392 less C_2 in dormancy. Interestingly, these hotspot parameter values indicate that vegetation cover

393 mainly captures a higher and wider hotspot in maturity, but a lower and narrower hotspot in

394 dormancy in the red band. In the NIR band, vegetation cover mainly captures a lower but wider

395 hotspot in maturity, and a higher and narrower hotspot in dormancy. Such hotspot behaviors

396 should result from the leaf-on and leaf-off status in combination with spectral multiple scattering

20

397   effects within vegetation canopy in red and NIR bands. This provides direct evidence on the

398   spectral variability of the hotspot effect with respect to vegetation phenology.

399   As a comparison, Figure 4 (lower left) presents the average NDVI as a function of IGBP

400   class in maturity and dormancy seasons. NDVI values are generally bigger in maturity than in

401   dormancy for most IGBP classes. This indicates that the selected IGBP classes for this

402   phenological analysis are mainly in a leaf-on and leaf-off stage, respectively. Notably, the NDVI

403   values are very close for few classes (e.g. Shrubland, Woody Savannas and Urban), likely due to

404   the lack of green foliage across classes. Figure 4 (lower right) presents the fit-RMSEs by the

405   RTCLSR model for maturity and dormancy seasons in the red and NIR bands. The fit-RMSEs

406   are chiefly higher in the NIR than in the red, but do not show significant differences between

407   these two seasons. This comparison reveals that NDVI alone doesn't distinctly capture this type

408   hotspot variation as was detailed by using two hotspot parameters.

409   Figure 4 near here

4.1.2. Hotspot BRFs

411   The scatterplots in Figure 5 (top panel) show the agreement between model-predicted and

412   observed hotspot BRFs in the red and NIR bands for the entire POLDER database. The

413   correlations between the two are very high ($R^2 > \sim 0.90$) in both the red and NIR bands. In the red

414   band, the Maignan method slightly underestimates the hotspot BRF; particularly at a range of

415   low reflectances (i.e., bias = -0.005 for BRFs < 0.1), but overestimates hotspot BRFs at a range

416   of high reflectances (i.e., bias = 0.011 for BRFs ≥ 0.4). In the NIR band, the Maignan method

417   overestimates hotspot BRFs by 0.014 units at a range of BRFs ≤ 0.3, and by 0.008 at range of

418   BRFs > 0.4. These biases are slightly corrected by using the RTCLSR model. Although the

419   RTCLSR model with two free parameters fits the hotspot BRFs a little better than the Maignan

420   method, the differences between them in fitting observed BRFs in the close proximity of hotspot

421   direction (i.e., $\xi \leq 1.5°$) were minor.

422   To further examine these two models in fitting hotspot BRFs as a function of surface type,

423   we selected four IGBP classes to reflect a forest, mixed, grass, and sparsely vegetated gradient

424   representing different canopy physiognomies and structures. In the red band, the Maignan

425   method tends to underestimate the hotspot BRFs by 0.014 units for the 'Evergreen Needleleaf

426   Forest' (ENF) class. The underestimation is reduced to 0.011 units for the 'Woody Savannas'

427   (WSa) class, and the model fits well (underestimates by 0.003) for the 'Grasslands' (GrL) class;

428   but somewhat overestimates by 0.009 units for the 'Barren or Sparsely Vegetated' (BSV) class.

429   The relative average difference (RAD) between these two model reaches to 12% for ENF class.

430   These biases are generally corrected by using the RTCLSR model (Figure 5). In the NIR band,

431   the biases in reconstructing hotspot BRFs by Maignan method are -0.007 for ENF, 0.001 for

432   WSa, -0.017 for GrL, and 0.018 for BSV. These biases are reduced to the range from -0.001 to

433   -0.003 by using the RTCLSR model. This demonstrates that the RTCLSR model can provide

434   further improvement for hotspot-fits for a subset of IGBP classes.

435   Figure 5 near here

436   To qualitatively compare the Maignan and RTCLSR models, Figure 6 presents model

437   predicted and observed BRFs for the ENF class as a function of phase angle in the proximity of

438   the principal plane in 6 bands. We only use the observations falling within the shaded area in

439   Figure 1 (a) to approximate the principal plane. Data sources are marked on each subplot with a

440   SZA=44.89˚ recording the hotspot direction. The NDVI values can be directly derived from the

441   data sources. The optimized C_1 and C_2 values for the ENF class in the corresponding bands are

442   used for each data set. This figure shows that the Maignan method and the RTCLSR model

443   generally capture the hotspot signatures very well for these POLDER data; however, Maignan

444   method seems to overestimate the hotspot height and underestimate hotspot width in blue band,

445   but somewhat underestimate hotspot width in other bands for this dataset. The RTCLSR model

446   presents more flexibility for capturing the hotspot observations. This is one of the key features of

447   the RTCLSR model; i.e., its ability to leverage the reciprocal nature of anisotropic reflectances to

448   improve retrieval quality.

449   Figure 6 near here

450   **4.2. Hotspot parameter values for one tile of MODIS hotspot data**

451   We retrieve two hotspot parameter values using one tile of MODIS hotspot data (h20v11)

452   (Table 2). In general, C_1 values are larger in lower reflectance, which indicates relatively

453   prominent hotspot effects due to lack of multiple scatterings from vegetation cover, which shows

454   a consistent variation tendency with two hotspot parameter values for POLDER data. C_1 and C_2

455   values do not present significant differences between three major land cover types in this tile,

456   dominated by savannas. However, the optimized C_1 and C_2 values present some differences in

457   the corresponding bands between MODIS and POLDER, likely because MODIS hotspot data are

458   derived only from one tile. From Figure 1 (d), we can also see that the BRDF shapes

459   reconstructed using the Maignan (green curve) and RTCLSR models (black curve) in the NIR

460   band are very close except for the hotspot peak. The optimal $C_1=0.4$ for 2,275 MODIS data sets

461   in this tile characterizes a low hotspot height, compared with the Maignan method for this

462   extreme example. Note that the MODIS has difficulty in acquiring sufficient hotspot signatures

463   on a global scale. As such, analysis of potential scale inconsistencies between MODIS and

464   POLDER was not comprehensively performed using current hotspot data.

4.3. Results with in-situ and airborne data

466   We used airborne CAR SCAR-B cerrado and forest measurements (Tsay et al, 1998), as

467   well as two high-quality field BRDF data sets (Iron et al., 1992; Deering et al., 1999) to evaluate

468   the RTCLSR approach. Measurements are limited in the proximity of the principal plane, and

469   hotspot observations are selected for $\xi \leq 1.5°$ according to our sampling design (Figure 1, a). The

470   CAR cerrado dataset was collected on a forest-grass vegetation system that is known for its

471   distinct hotspot signature in the red and NIR bands. Dense forest covered by tall trees with a

472   close canopy had two-flight measurements. For these data sets, we only make use of the band

473   where the hotspot signature was the most prominent.

474   Using CAR SCAR-B cerrado measurements, Figure 7 presents the model predicted and

475   observed BRFs in the red and NIR bands (not shown for the RTLSR model). We provide three

476   specific cases to identify the potential difference between these two methods. Figure 7 (a-b)

477   present the optimalized C_1 and C_2 for the RTCLSR model for this specific data set. Figure 7 (c-d)

478   use the $C_1 = 1.0$ and $C_2 = 3°$ as default values because K_{RTC} with the default C values captures a

479   very close kernel shape with K_{RTM} (Figure 2). Figure 7 (e-f) present two-model consistencies by

480   adjusting two hotspot parameters of the RTCLSR model to approach to Maignan predicted

481 shapes for this specific data set (observations not shown). This comparison shows that the

482 RTCLSR model with two free hotspot parameters can approach to Maignan method to a very

483 great degree. Using CAR SCAR-B forest measurements, we compared the difference between

484 the model-predicted and observed BRFs in the principal plane, and over the entire viewing

485 geometries between two models (Figure 8). The difference in reconstructing the hotspot BRFs

486 between these two models are distinctly exhibited over the entire viewing hemisphere. We

487 further performed the statistical analysis for these two CAR datasets for BRFs near the hotspot

488 region of phase angle $\xi \leq 5°$ and within the viewing hemisphere of VZA $\leq 75°$ (Figure 9). While

489 these two approaches do not present difference for the entire CAR datasets, the significant

490 improvement occurs in recreating hotspot signatures using the optimized hotspot parameters of

491 the RTCLSR model for the RMSEs, biases and correlation coefficients (Figure 9).

492   Figure 7, 8 and 9 near here

493   Finally, we compared the RTLSR, RTCLSR, and Maignan models fits to the field

494 measurements collected from soil and vegetation surface (Figure 10). A C_1=0.4 and a C_2=5.2° are

495 the optimal values for the soil measurements in the red, and C_1=1.3 (C_2=10°) and C_1=1.0

496 (C_2=8.0°) capture the best hotspot-fits for the black spruce (*picea mariana*) in the red and NIR

497 bands. Results indicate a significant difference between the model-predicted hotspot BRFs for

498 the soil and the black spruce surfaces. The RTCLSR model with a C_1=1.0 reconstructs the

499 hotspot height for the black spruce as same as Maignan method; but a C_2=8.0° can characterize a

500 wider hotspot for matching this measurement in the NIR band. The old back spruce captures a

501 more prominent hotspot signature in the red than in the NIR. For the in-situ data, the fit-RMSEs

25

502   for the RTLSR, the Maignan and the RTCLSR are 0.0073, 0.0067 and 0.0058 in the red, and

503   0.0530, 0.0515 and 0.0506 in the NIR, respectively. Since these models are consistent in fitting

504   these measurements except for hotspot region, the difference in overall fit-RMSEs results from

505   their hotspot effects.

506   <center>Figure 10 near here</center>

4.4. Sensitivity of hotspot parameters

508   To examine the sensitivity of hotspot parameters to hotspot-fits, we provide the plots

509   showing the fitting errors (color contour) as functions of C_1 and C_2 at each iteration for the entire

510   POLDER sampled dataset in the red and the NIR bands (Figure 11, top). Results indicate that the

511   C_1 values are more sensitive to hotspot-fit than C_2, because the fitting errors change more rapidly

512   along C_1 than C_2. For a given C_2, fitting errors present certain symmetry about C_1 because large

513   or small C_1 values generate the comparable magnitude of fitting errors. The minimum RMSE

514   occurs at the optimal C_1 and C_2 values (the white point). Similar results were found across IGBP

515   classes.

516   Since the BRDF sampling can have an effect on the sensitivity of model parameter

517   retrievals for kernel-driven models (Lucht et al., 2000), we also examined the sensitivity of the

518   two hotspot parameters to the model parameters. To do this, we evaluated the modeled hotspot

519   reflectance as a function of C_1 (taking $C_2 = 3°$ as the default value) for three sample sizes (i.e., 12,

520   60 and 161 measurements) in principal plane. These BRDF observations are sampled from the

521   airborne CAR cerrado measurements, which contained 29,160 BRF samples. In each case, 6

522   uniformly-distributed observations in the vicinity of the hotspot region (i.e., $\xi \leq 5°$) were used,

<center>26</center>

523   and the rest of the observations outside of this hotspot region were randomly sampled.

524   Figure 11 (bottom) presents the sensitivity of modeled hotspot reflectance as a function of

525   C_1 in the red band ($C_2 = 3°$). This figure demonstrates that the BRDF sample sizes have a certain

526   effect on the sensitivity of the C_1 values to the modeled hotspot BRFs, since the hotspot BRFs as

527   a function of C_1 values presents varying slopes for these three cases of BRDF sample sizes. This

528   leads to slightly varying C_1 values, even when using identical hotspot observations for different

529   total BRDF sample numbers. However, the variation range of the modeled BRFs as a function of

530   C_1 can effectively cover the observed hotspot peak (i.e. HS$_{\text{BRF}}$ = 0.23). Result also indicate that

531   the modeled hotspot BRFs, using the Maignan method, are sensitive to the total BRDF sample

532   numbers in this examination; but with a slight overestimation of the hotspot BRFs. This is

533   consistent with result shown for the NIR band when using MODIS, POLDER and CAR.

534   This investigation demonstrates that the sensitivity of hotspot parameters is somewhat

535   related to varying BRDF sample numbers, which in turn tend to have an effect on model

536   parameter retrievals. This effect holds true even when using the same observations in the vicinity

537   of the hotspot direction (i.e., $\xi \leq 5°$). This implies that the model predicted hotspot BRFs using a

538   set of optimalized prior C_1 and C_2 values in RTCLSR model (combining K_{LSR} and K_{RTC}) would

539   be sensitive to the three model parameters (i.e., f_{iso}, f_{geo} and f_{vol}) to a certain extent that the

540   adjustment of hotspot BRF dynamics by three model parameters is no longer effective. In such a

541   situation, the two free hotspot parameters in RTCLSR model provide an improved capacity to

542   capture more accurate hotspot signatures.

543   Figure 10 near here

4.5. Influence on retrieval of intrinsic albedo and clumping index

To evaluate the performance of the RTCLSR method for potential applications, we evaluated the retrieval of intrinsic albedos and clumping index (CI) from available POLDER and MODIS data. The BSA values were calculated for SZAs ranging from 0° to 75° at the interval of 15°. In general, the intrinsic albedo retrievals between the RCLSR and RTCLSR models are in a very high correlation for both POLDER ($R^2 = \sim 1.0$) and MODIS ($R^2 > \sim 0.9$) data; with negligible biases ($< \sim 0.0003$ in red and $< \sim 0.0006$ in NIR), while the difference in CI values between models was rather significant (Table 1 and Figure 12). As compared with the RTCLSR model results, a major overestimation of CI values occurs with the RTLSR model, but a slight underestimation of CI values occurs with the Maignan method. This is attributed to the difference in reconstructing hotspot BRFs between models. Figure 12 exhibits the scatter plots between models for ~11,632 CI values for 15 IGBP classes in the NIR (Figure 12, a-b) and the red bands (Figure 12, c-d) using POLDER data. According to the CI inversion algorithm, the CI biases between models (despite a high correlation, $R^2 = \sim 0.9$) result from biases in modeling hotspot BRFs. For most IGBP classes from POLDER data, about 20% of the relative average difference (RAD) in retrieving CIs occurs between the RTLSR model and the RTCLSR model, while about 10% of RAD occurs between the Maignan method and the RTCLSR in the NIR (Table 1). In the red band (Figure 12, c-d), the RAD in CI retrievals between the Maignan method and the RTCLSR model is generally small, while it still remains about 20% between the RTLSR and the RTCLSR. For the MODIS data, the RAD in CI retrievals arrive at about 6% and 12% in the red and the NIR bands between the RTCLSR and the Maignan (Figure 12, e-f).

28

565   Notably, we use more measurements in CI estimates because we can, in theory, reconstruct the

566   hotspot BRFs using two prior IGBP-based hotspot parameter values that are derived from the

567   high-quality observations in Section 4.1.1. In addition, we merely compare the retrieved CI

568   values between models following the objective of this paper. To extensively validate these CI

569   estimates with ground measurements would require the expanded use of additional

570   measurements beyond the ones used in this study.

571   5. Conclusions and discussion

572   In this study, we proposed a new method to correct the hotspot effects for the RTLSR model

573   known for its use within the operational MODIS BRDF/Albedo product. The method makes use

574   of the exponential function with two free parameters (C_1 and C_2) to characterize hotspot height

575   and width. Our results indicate that, although the Maignan method with no free hotspot

576   parameters characterizes the hotspot effect in a relatively high accuracy (particularly for

577   POLDER), the RTCLSR model can provide a further improvement in hotspot-fits. This is mainly

578   attributed to the two free hotspot parameters that can be adjusted to reach their optimal values for

579   the near-hotspot measurements available. Further analysis of the two hotspot parameters using

580   hotspot data reveals that the hotspot signatures are somewhat related to surface type and

581   vegetation phenology for available POLDER data. We found that the hotspot height (C_1) value is

582   bigger in the red band than in the NIR band for most vegetation types, indicating a more

583   prominent hotspot in the red band possibly due to the strong chlorophyll absorption of vegetation

584   foliage.

585   The RTCLSR model is quite consistent with the other two models in the intrinsic albedos

586   retrievals, but is somewhat different in CI retrievals through the use of the inversion algorithm of

587   Chen et al. (2005). This reveals that the albedo retrievals using the RTCLSR would be consistent

588   with the archived albedo product using the routine RTLSR algorithm; however, the RTCLSR

589   model would provide more accurate hotspot signatures that may lead to an improved

590   understanding of vegetation biophysical parameter retrievals in relation to hotspot BRFs. A

591   similar analysis of the RTCLSR with the MODIS hotspot data, airborne CAR data and field

592   measurements reveals the broad adaptability of this new method for different spatial resolutions;

593   however, further investigation into the scale issue of hotspot effect using the RTCLSR model is

594   still a challenge mainly due to the lack of sufficient hotspot data at different spatial resolutions.

595   Investigation into the sensitivity of these two hotspot parameters shows that C_1 is more sensitive

596   to hotspot-fits than C_2. The total BRDF sampling design can also play a role on the sensitivity of

597   the hotspot parameters to hotspot-fits, because the total sample numbers (even having a good

598   distribution) can have an effect on the model parameter retrievals, in particular the sparse BRDF

599   sampling cases typified by the MODIS retrieval.

600   The original design of the kernel-driven linear Ross-Li BRDF model comprised a collection

601   of kernels for different scenarios of land surface types. Thus, kernel functions are derived from

602   different assumptions for vegetation canopy structures, and view and illumination geometries.

603   These assumptions may result in differences in modeling the radiation field (Wanner et al., 1995)

604   especially in the hotspot direction (Huang & Jiao et al., 2012). Methodologically, the exponential

605   approximation of this hotspot kernel function may also be used to correct the other volumetric

606   scattering kernel (i.e., RossThin), because this exponential hotspot function makes use of two

607 free parameters (C_1 and C_2) to fit hotspot signatures, rather than use surface biophysical

608 parameters as inputs to drive a theoretical hotspot model. The exponential function form is

609 rooted in gap probability theory and has been one of major contributions to hotspot modeling

610 (Qin et al., 1995). The corrected volumetric kernel can be combined with various geometric

611 optical kernels for potential applications. However, the use of multi-kernel combination models

612 would require recalibration of the C_1 and C_2 parameters.

613   In the situation where hotspot signatures are not available, the C_1 and C_2 values would need

614 to be estimated on an *a priori* basis for it to initialize an RTCLSR model inversion. This has been

615 attempted by fitting the hotspot data of several spatial resolutions via two means. Globally

616 optimized C_1 and C_2 values can characterize the overall accuracy of the hotspot effect for certain

617 satellite hotspot data, while variable-related optimized C_1 and C_2 values can help explore hotspot

618 variation as a function of some underlying variables such as surface type and vegetation

619 phenology. We found that a prior $C_1 = 1$ and $C_2 = 3°$ provide a stable initialized value in the

620 RTCLSR model that is comparable in performance to the Maignan method.

621   Because the hotspot effect is very sensitive to the phase angle between the view and

622 illumination in the retro-solar direction (Bréon et al. 2002), its analysis for remote sensing

623 applications requires a very high geometric accuracy. This implies that it is especially difficult to

624 capture accurate hotspot observations in field measurements due to the shadows of the

625 goniometer and sensors that must have a small enough IFOV (e.g., $\leq 1°$). Use of the field

626 measurements with an IFOV= $15°$ in this study aims to stress that the reciprocal nature allows

627 the RTCLSR model to acquire hotspot-fits with the least RMSEs for this data set. However, with

628   two free hotspot parameters determined *a priori* by using enough hotspot data, this new method

629   provides an improved understanding of the hotspot effect, and thus has potentials for certain

630   ecological applications in regard to the hotspot BRFs for complex heterogeneous environments.

631

6. Appendix A

The shaded area in Figure 1 (a) contains four parts. As the 1st constraint, all observations falling within the phase angle having the radius of R should be included in set **A**. Here, $R = 1.5°$ is used, but R can be adjusted properly for different hotspot data.

$$\mathbf{A} = \left\{ \xi \middle| \xi \leq R \right\}$$

To select the observed BRFs close to principal plane (PP) for visually comparing with modeled BRFs in PP, we define the distance, H, which is perpendicular to the principal plane, as the 2nd constraint. Obviously, a less H value can select observations in the shaded area to get closer to PP. This generates set **B** as follows. Here, $H = 10°$ is attempted for MODIS and POLDER data, but $H = 1°$ is attempted for airborne CAR and field data.

$$\mathbf{B} = \left\{ \varphi \middle| | \theta_v \sin \varphi | \leq H \right\}$$

As the 3rd constraint, we should consider that, in a 2-D plot that exhibits the observed BRFs in approximate PP, spurious visualizations, particularly in the proximity of hotspot direction in PP, possibly result from some observed BRFs that are not actually near hotspot region in PP, e.g., a $H = 10°$ without other constraints will allow the observed BRFs in the unshaded sector domain taking Sun as the center (Figure 1, a) to be exhibited as near-hotspot BRFs in PP. To remove these observations in 2-D plots that present observed and modeled BRFs in approximately PP (e.g., Figure 1, d), we define an intersection angle (θ) between PP line and the line passing through Sun (Figure 1, a), and derive set **C** and set **D** as follows. Here, $\theta = 45°$ is attempted for these hotspot data used in this study.

652 $$\mathbf{C} = \left(\left\{ \varphi \left| \frac{\sin\theta}{\sin(\pi-\varphi-\theta)} > \frac{\theta_v}{\theta_s} \right. \right\} \cup \left\{ \varphi | \varphi \ge \pi - \theta | \right\} \right) \cap \left\{ \varphi | \theta_v \cos\varphi < \theta_s \right\}$$

653 $$\mathbf{D} = \left(\left\{ \varphi \left| \frac{\sin\theta}{\sin(\theta-\varphi)} < \frac{\theta_v}{\theta_s} \right. \right\} \cap \left\{ \varphi | \varphi < \theta | \right\} \right) \cap \left\{ \varphi | \theta_v \cos\varphi > \theta_s \right\}$$

654 Finally, the shaded area in Figure 1 (a) can be derived by implementing set operation for four

655 sets above:

656 $$\mathbf{A} \cup \left(\mathbf{B} \cap (\mathbf{C} \cup \mathbf{D}) \right)$$

657

7. Acknowledgments

665 Table.

666   Table 1. Statistics of the clumping index values retrieved by three models

Class	Number	RTLSR		Maignan		RTCLSR		(RTLSR- RTCLSR)	(Maignan-RTCLSR)
		Mean	Std.	Mean	Std.	Mean	Std.	/ RTCLSR (%)	/RTCLSR (%)
ENF	793	0.57	0.04	0.49	0.03	0.51	0.04	13.09	4.32
EBF	898	0.76	0.08	0.56	0.06	0.64	0.07	19.02	11.85
DNF	219	0.66	0.02	0.57	0.02	0.59	0.02	10.54	4.29
DBF	682	0.80	0.06	0.63	0.05	0.67	0.05	19.59	6.89
MiF	690	0.76	0.10	0.57	0.08	0.63	0.09	21.55	9.02
CSh	549	0.77	0.08	0.58	0.06	0.63	0.07	22.83	7.22
OSh	1247	0.86	0.10	0.68	0.10	0.74	0.10	16.31	8.68
Wsa	1035	0.83	0.06	0.62	0.06	0.68	0.06	22.49	8.32
Sav	734	0.87	0.06	0.67	0.06	0.74	0.06	17.64	10.11
GrL	1075	0.88	0.09	0.68	0.10	0.76	0.10	16.21	9.56
Pwe	21	0.95	0.06	0.65	0.05	0.77	0.05	22.29	15.68
CrL	960	0.89	0.07	0.67	0.06	0.75	0.06	19.55	10.48
Ubu	835	0.84	0.06	0.65	0.06	0.72	0.06	17.20	10.13
CNVM	727	0.89	0.06	0.66	0.05	0.75	0.05	19.00	10.94
BSV	1167	0.99	0.16	0.85	0.19	0.92	0.17	8.00	7.44

667

668

669

670 Table 2. The globally optimized C_1 and C_2 values derived from one $10° \times 10°$ tile (h20v11) of MODIS

671   surface reflectance products (MOD09 and MYD09) in 7 reflected solar bands

Band	Band1	Band2	Band3	Band4	Band5	Band6	Band7
(nm)	(620-670)	(841-876)	(459-479)	(545-565)	(1230-1250)	(1628-1652)	(2105-2155)
C_1	0.7	0.4	0.7	0.7	0.6	0.7	0.7
C_2 (°)	5.2	4.5	5.2	5.2	3.5	5.2	5.2

672

673

674

Figure Captions

Figure 1. (a) The method to select observations near principal plane and in the proximity of hotspot direction to be showed in 2-D plots, its formulation is detailed to appendix A; (b) spatial distribution of view and sun geometries for a typical POLDER data set, i.e., IGBP_01_200609brdf_ndvi08. 0824_1671, and (c) for a typical MODIS data set in h20v11 for savanna; (d) the observed and modeled BRFs using Maignan method, and RTCLSR model with C_1=0.4, and C_2=4.5° as a function of phase angle for this MODIS data in the NIR. A minus sign is assigned to the phase angle when $\theta_v \cos\varphi < \theta_s$

Figure 2. LiSparseReciprocal kernel (K_{LSR}) at SZA of 15°, 30°, 45° and 60° (top) and three volumetric kernels in PP (bottom). In the top subplot, the red and magenta dashed curves around the red solid curve are from different h/b and b/r ratios in K_{LSR}. The red solid curve is for the operational K_{LSR} that adopts h/b=2 and b/r=1; red dashed curve is for h/b=2 and b/r=1.2; magenta dashed curve is for h/b=2.5 and b/r=1. In the bottom subplot, three volumetric kernels are for the operational RossThick kernel (K_{RT}, black curve), the Maignan kernel (K_{RTM} with green solid curve for $\xi_0 = 1.5°$ and green dashed curve for ξ_0 = 3.0°), and RossThickChen kernel (K_{RTC}) with C_1=1 and C_2=3° (red dashed curve). The upwardly-shifted K_{RTC} with C_1=1 and C_2=3° (red solid curve), C_1=1 and C_2=5° (blue dashed curve), and C_1=0.6 and C_2=3° (magenta dashed curve) for a SZA=30° is aligned with the K_{RT} and K_{RTM} for a convenient comparison.

Figure 3. The globally optimized C_1 and C_2 values, and the fit-RMSEs derived from the entire POLDER BRDF data in 6 bands (top); the C_1 and C_2 values (middle) and the correponding fit-RMSEs (bottom) for underlying IGBP class. The dashed lines (top right) present the relative fit-RMSEs (right ordinate) between Maignan method and RTCLSR model. 16 IGBP classes are Evergreen Needleleaf forest (ENF),

696   Evergreen Broadleaf Forest (EBF), Deciduous Needleleaf Forest (DBF), Deciduous Broadleaf Forest

697   (DBF), Mixed Forest (MiF), Closed Shrublands (CSh), Open Shrublands (OSh), Woody Savannas (WSa),

698   Savannas (Sav), Grasslands (GrL), Permanent Wetlands (PWe), Croplands (CrL), Urban and Build-up

699   (UBu), Cropland/Natural Vegetation Mosaic (CNVM), Barren or Sparsely Vegetated (BSV). Snow and

700   Ice (SI) is excluded from this study because of its strong forward scattering.

701   **Figure 4.** Two hotspot parameters (top) as a function of IGBP class in terms of the timing of Jun-Jul-Aug/

702   Dec-Jan-Feb in the northern hemisphere to represent maturity and dormancy season, respectively

703   (opposite in southern hemisphere) in the red and the NIR bands. The corresponding average NDVI and

704   fit-RMSEs (bottom) are presented as a comparison.

705   **Figure 5.** Comparison of the model predicted and observed hotspot BRFs for the entire POLDER BRDF

706   data (upper panel), and two IGBP classes for ENF and WSa (lower panel) in the red band.

707   **Figure 6.** POLDER observatoins (red points) and the reconstructed BRDF shapes by Maignan (green)

708   and RTCLSR model (black) in 6 bands for the ENF as a function of phase angle in terms of the sampling

709   design (i.e., Figure 1, a)

710   **Figure 7.** Comparison of Maignan with RTCLSR model using CAR/SCAR-B cerrado measurements in

711   principle plane in the red and the NIR bands. We elaborate on the differecnes between these two models

712   in terms of three cases: (a) and (b) show RTCLSR with the optimal C_1 and C_2 in case 1; (c) and (d) show

713   RTCLSR using $C_1 = 1$ and $C_2 = 3°$ as default values in case 2; (e) and (f) adjust RTCLSR model to

714   approach to Maignan result for deriving the opitimal C_1 and C_2 values in case 3.

715   **Figure 8.** Using CAR SCAR-B forests to examine the difference between model predicted and observed

716   BRFs in PP (top) and the difference between RTCLSR and Maignan over the entire viewing hemisphere

717   (bottom) using Flight # 1689 in the red (c) and using Flight # 1693 in the NIR (d).

718   **Figure 9.** Scatterplots showing the difference between modeled and observed BRFs near the hotspot

719   region ($\xi \leq 5°$, red points) and for the viewing hemisphere ($VZA \leq 75°$, black points), using CAR Flight #

720   1689 in the red band (a, b) and CAR Flight # 1693 in the NIR band (c, d)

721   **Figure 10.** Comparison of field soil measurements (top) and field old black spruce measurements (bottom)

722   with three models

723   **Figure 11.** The fitting errors as functions of C_1 and C_2 for the entire POLDER data in the red (left) and in

724   the NIR (right), and the white points on the contour plots represent the least fit-RMSEs with the optimal

725   C_1 and C_2 values; the modeled hotspot reflectance as a function of C_1 (given $C_2 = 3°$) using CAR data to

726   simulate three BRDF sample sizes (12, 60 and 161 samples) in the red band (bottom).

727   **Figure 12.** Comparison of CI retrievals between models using POLDER data in the NIR band (top) and in

728   the red band (middle), as well as using MODIS data (bottom) in the red and the in NIR bands. The dashed

729   and solid lines represent the one-to-one lines and the fitted lines, respectively.

730

731

732

733

Figure 1. (a) the method to select observations near principal plane and in the proximity of hotspot

direction to be showed in 2-D plots, its formulation is detailed to appendix A; (b) spatial distribution of

view and sun geometries for a typical POLDER data set, i.e., IGBP_01_200609brdf_ndvi08. 0824_1671;

(c) for a typical MODIS data set in h20v11 for savanna; (d) the observed and modeled BRFs using

Maignan method, and RTCLSR model with C_1=0.4, and C_2=4.5° as a function of phase angle for this

MODIS data in the NIR. A minus sign is assigned to the phase angle when $\theta_v \cos\varphi < \theta_s$

740

741

742
743
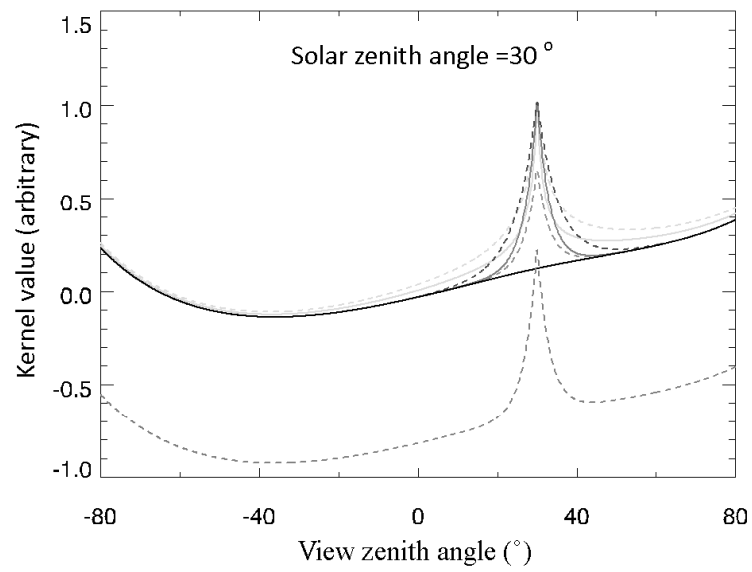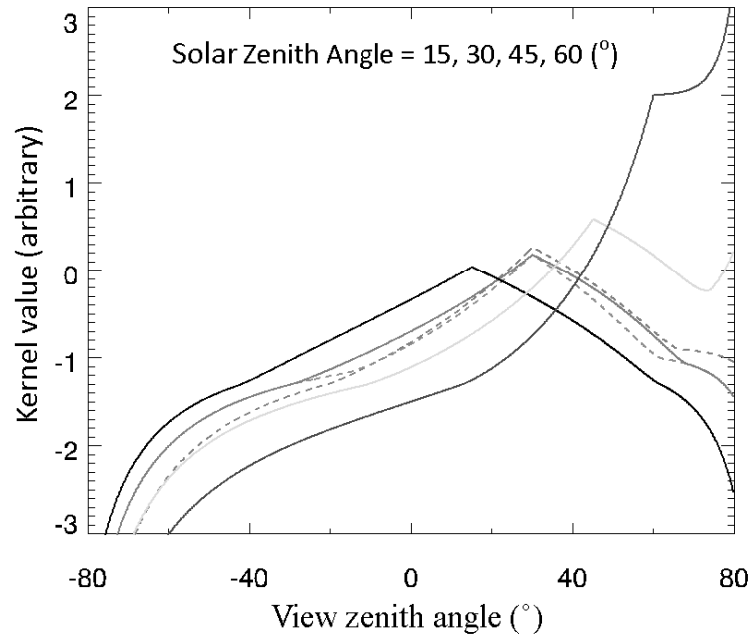
Figure 2. LiSparseReciprocal kernel (K_{LSR}) at SZA of 15°, 30°, 45° and 60° (top) and three volumetric

kernels in PP (bottom). Details are expounded in figure captions
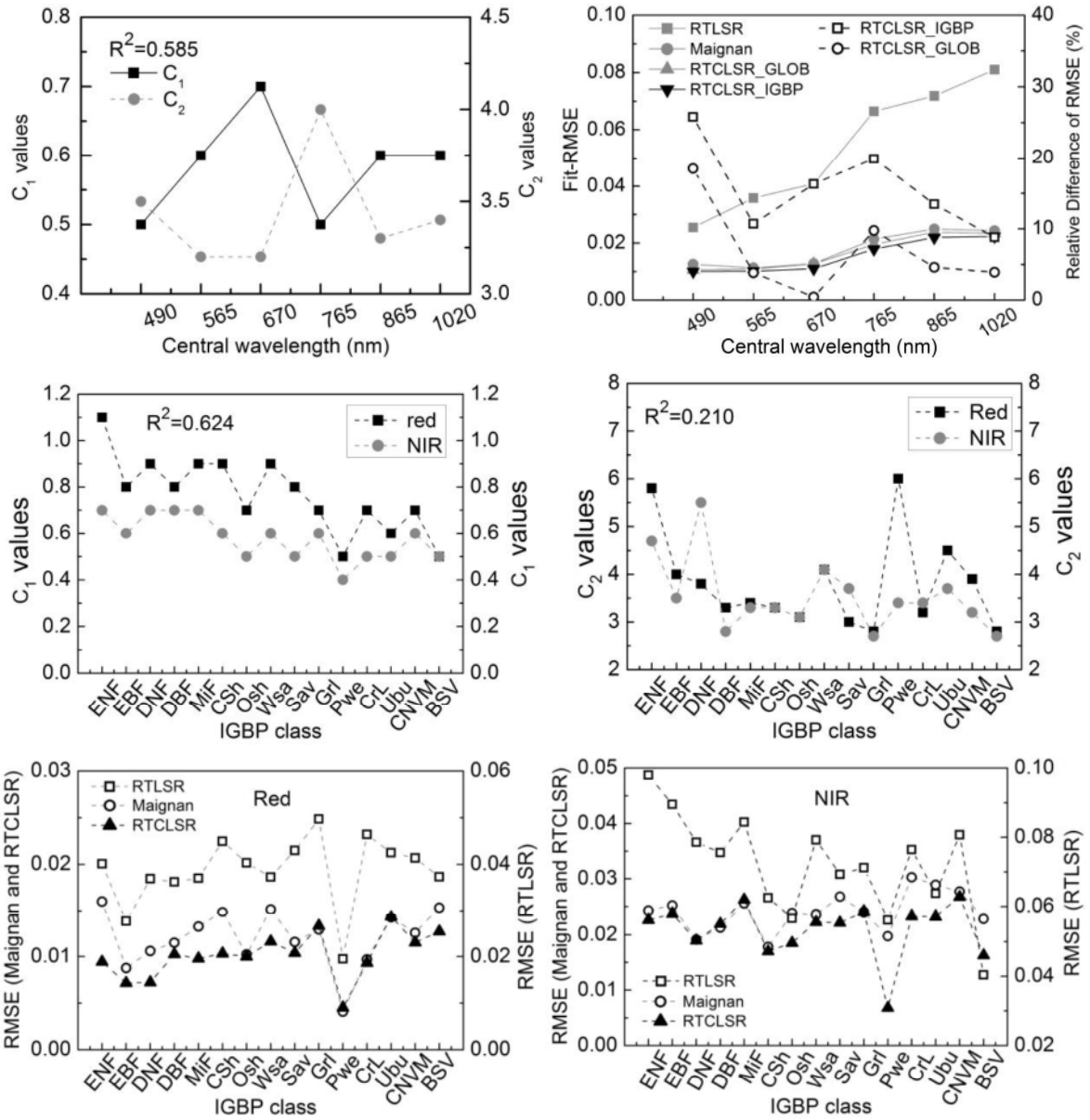
746

747

748

749

Figure 3. The globally optimized C_1 and C_2 values, and the fit-RMSEs derived from the entire POLDER

BRDF data in 6 bands (top); the C_1 and C_2 values (middle) and the correponding fit-RMSEs (bottom) for

underlying IGBP class. The dashed lines (top right) present the relative fit-RMSEs (right ordinate)

between Maignan method and RTCLSR model.

754

755

756
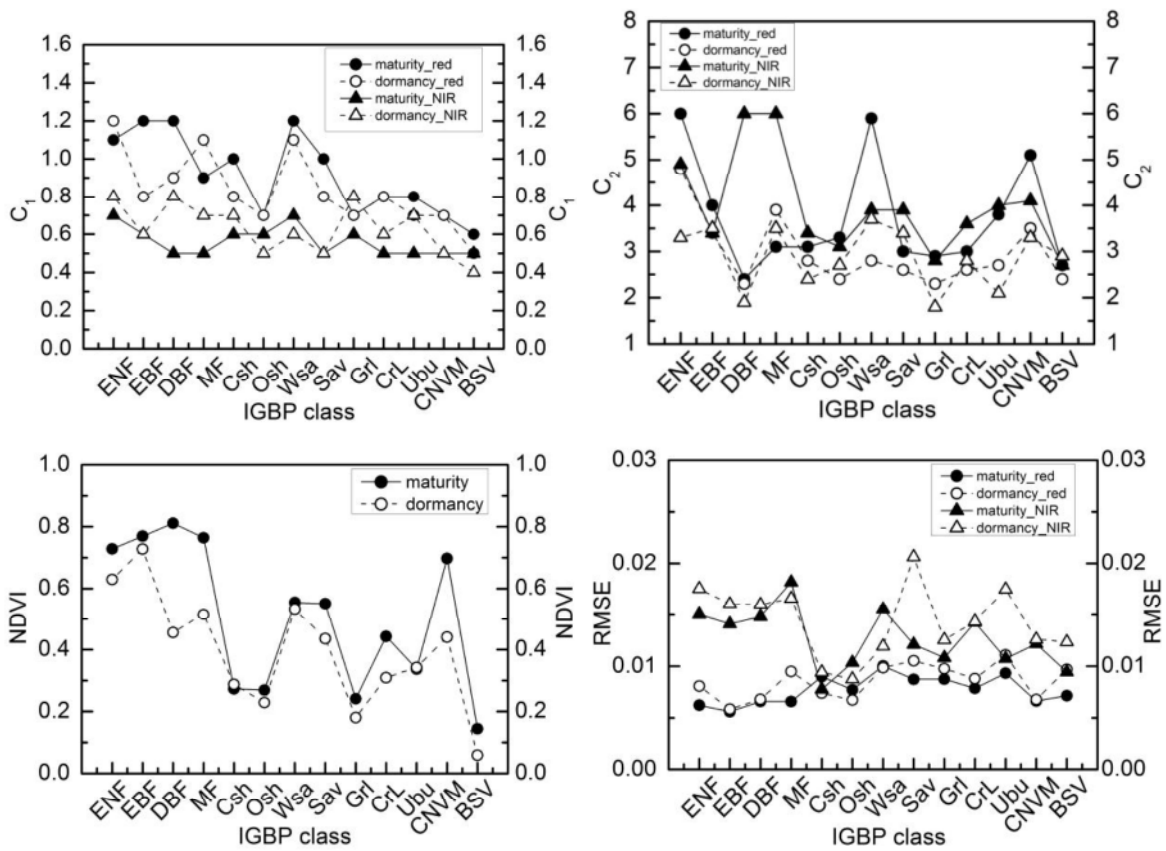
Figure 4. Two hotspot parameters (top) as a function of IGBP class in terms of the timing of

Jun-Jul-Aug/Dec-Jan-Feb in the northern hemisphere to represent maturity and dormancy season,

respectively (opposite in southern hemisphere) in the red and the NIR bands. The corresponding average

NDVI and fit-RMSEs (bottom) are presented as a comparison.

761

762
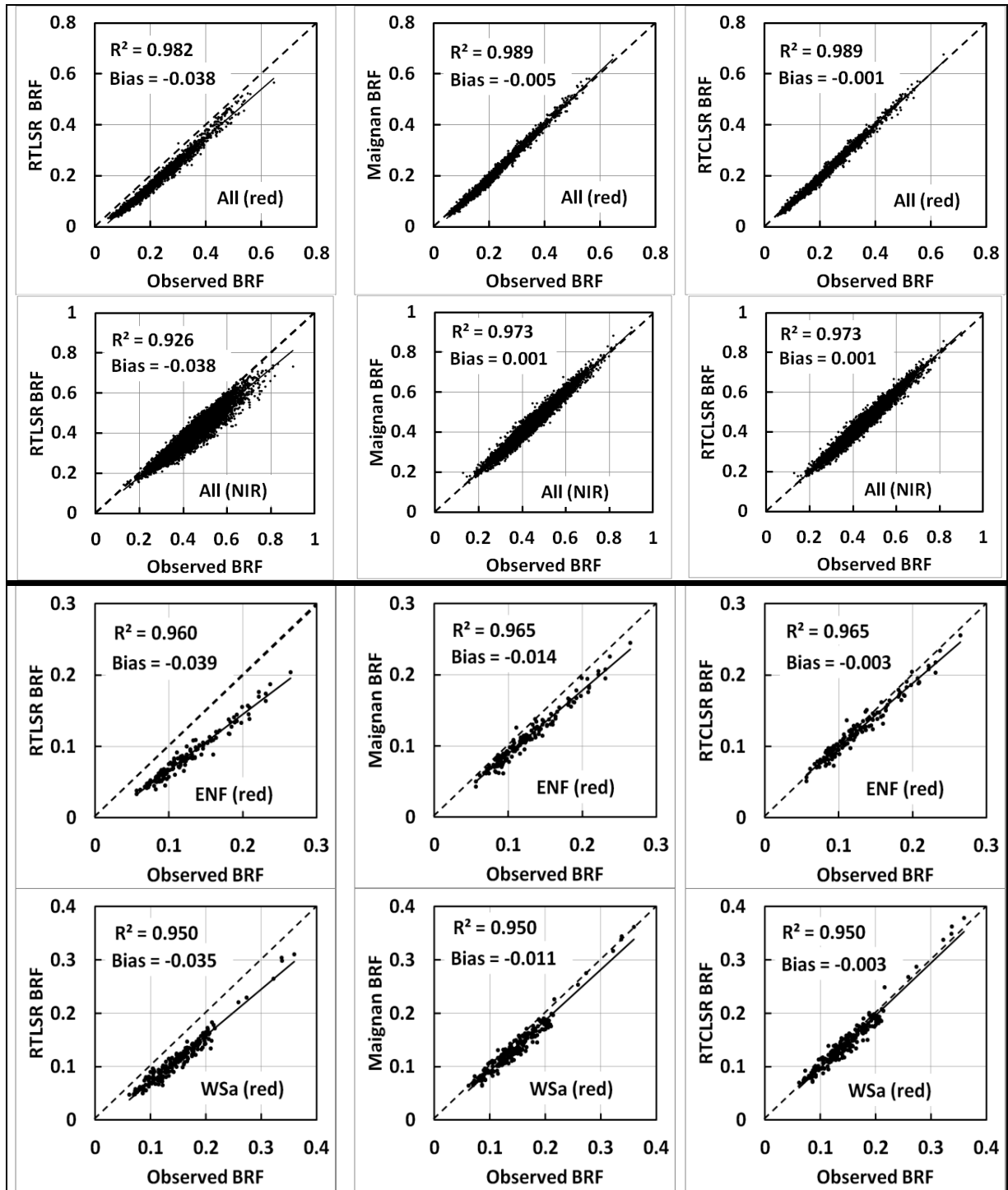
Figure 5. Comparison of the model predicted and observed BRFs for the entire POLDER BRDF data and

two IGBP classes, i.e., ENF and WSa in the red band.
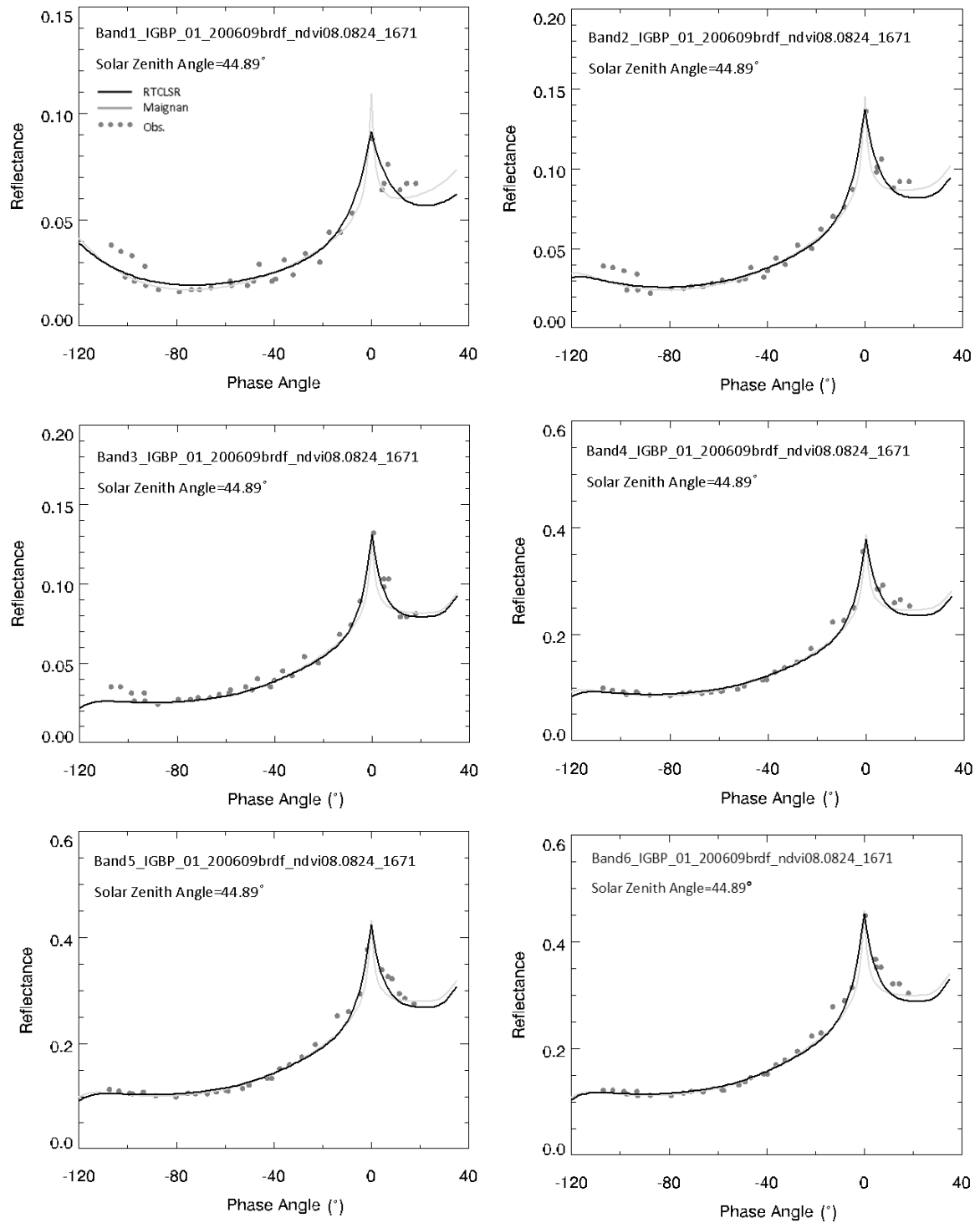
765

Figure 6. POLDER observatoins (red points) and the reconstructed BRDF shapes by Maignan (green)

and RTCLSR model (black) in 6 bands for the ENF class as a function of phase angle
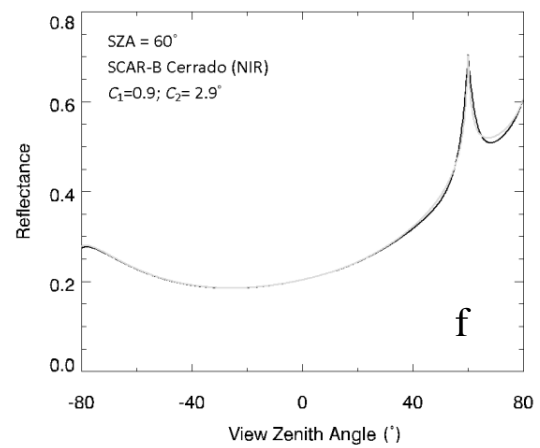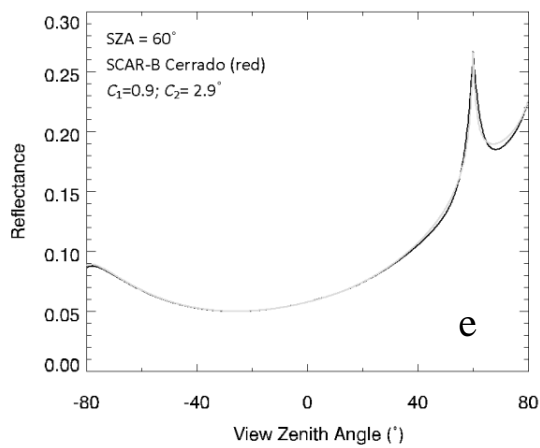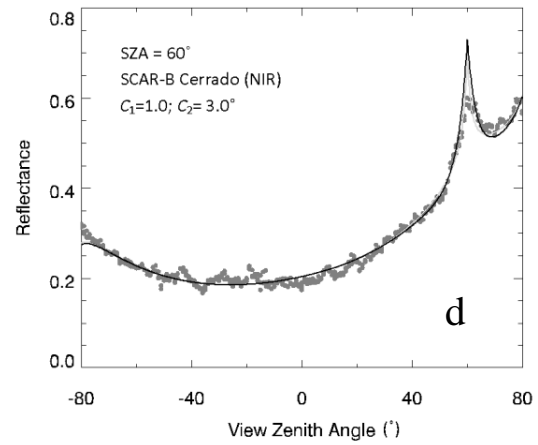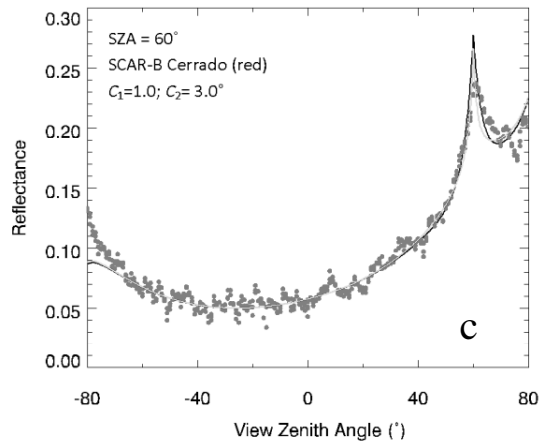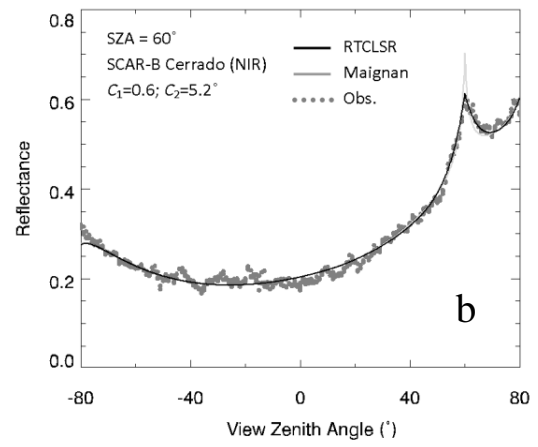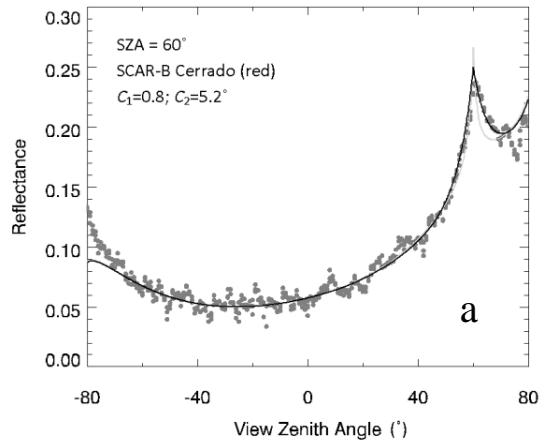
773

774

775
776

777 **Figure 7.** Comparison of Maignan with RTCLSR model using CAR/SCAR-B cerrado measurements in

778 principle plane in the red and the NIR bands. Details were expounded in figure captions.
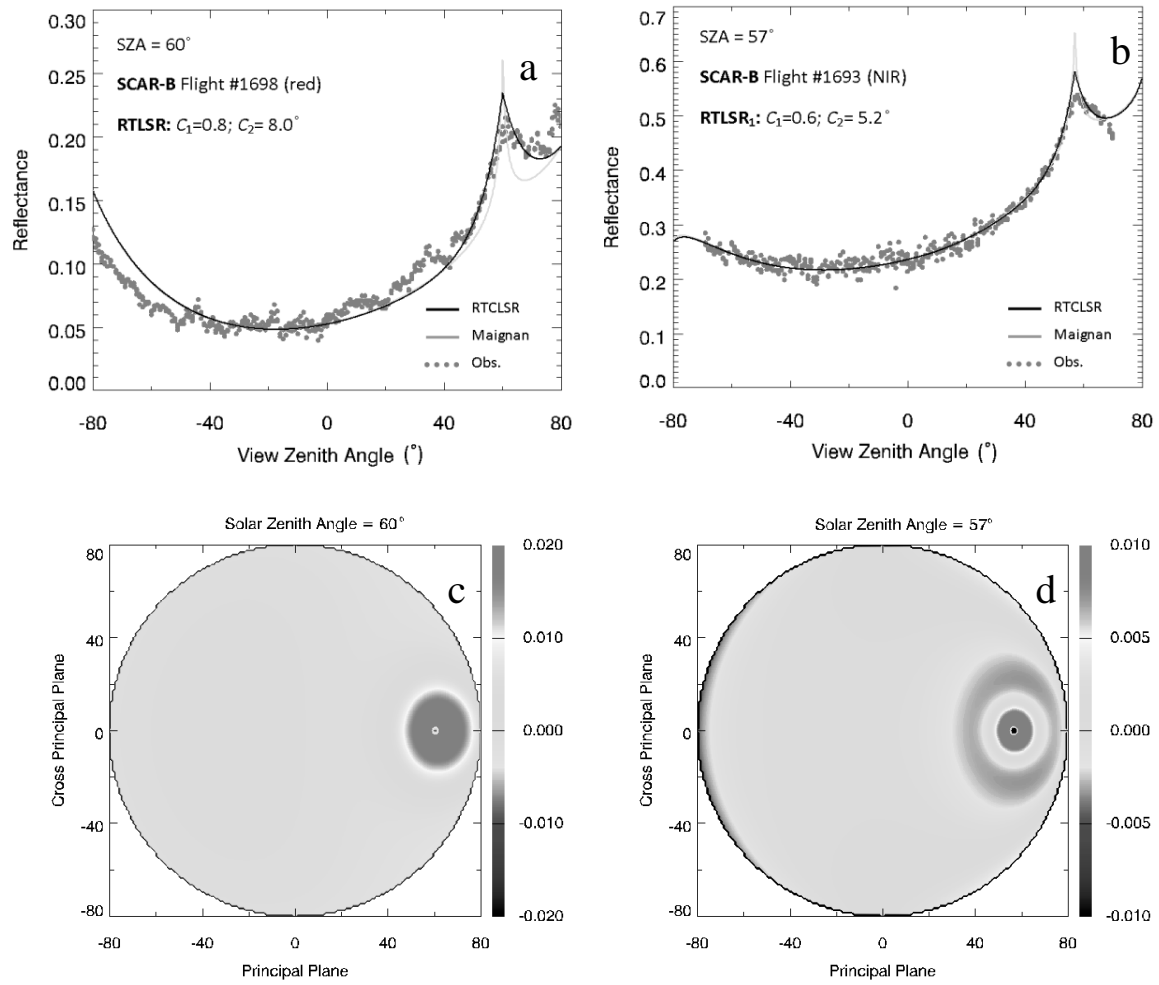
Figure 8. Using CAR SCAR-B forests to examine the difference between model predicted and observed

BRFs in PP (top) and the difference between RTCLSR and Maignan over the entire viewing hemisphere
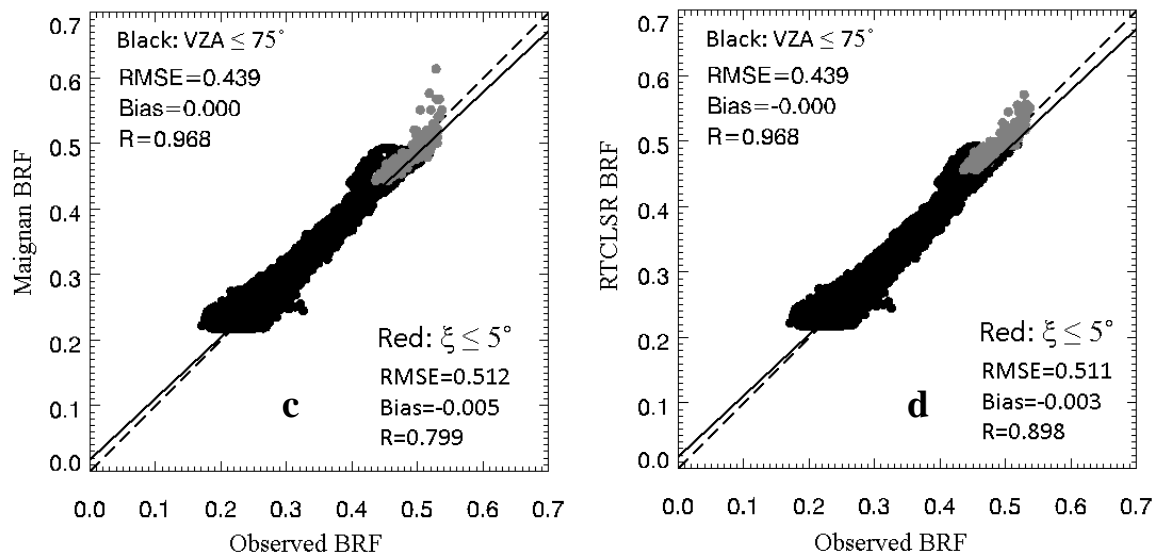
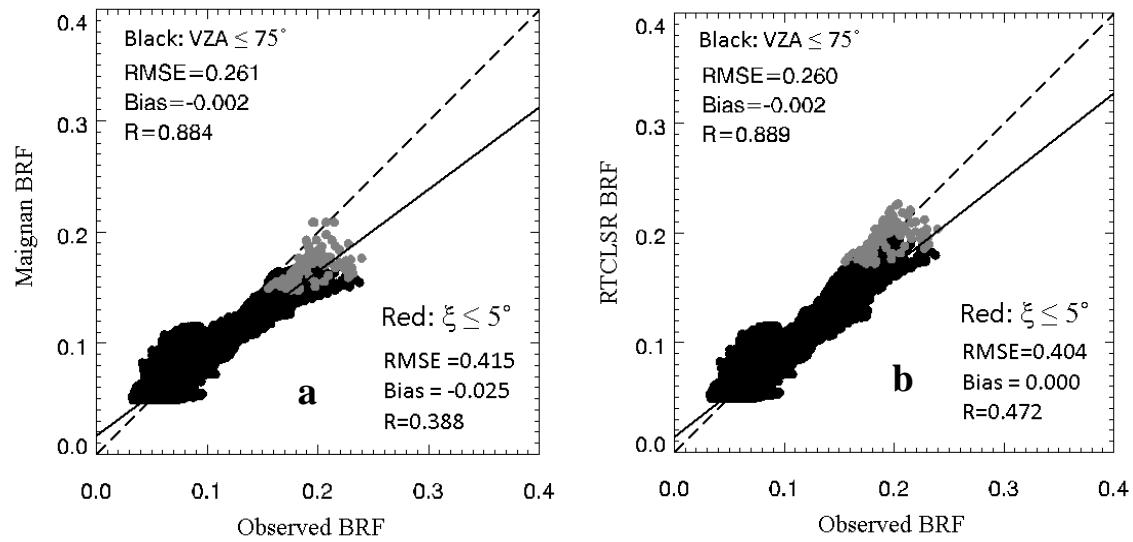(bottom) using Flight # 1689 in the red (c) and using Flight # 1693 in the NIR (d).

786

787

Figure 9. Scatterplots showing the difference between modeled and observed BRFs near the hotspot

region ($\xi \leq 5°$, red points) and for the viewing hemisphere (VZA $\leq$ 75°, black points), using CAR Flight #

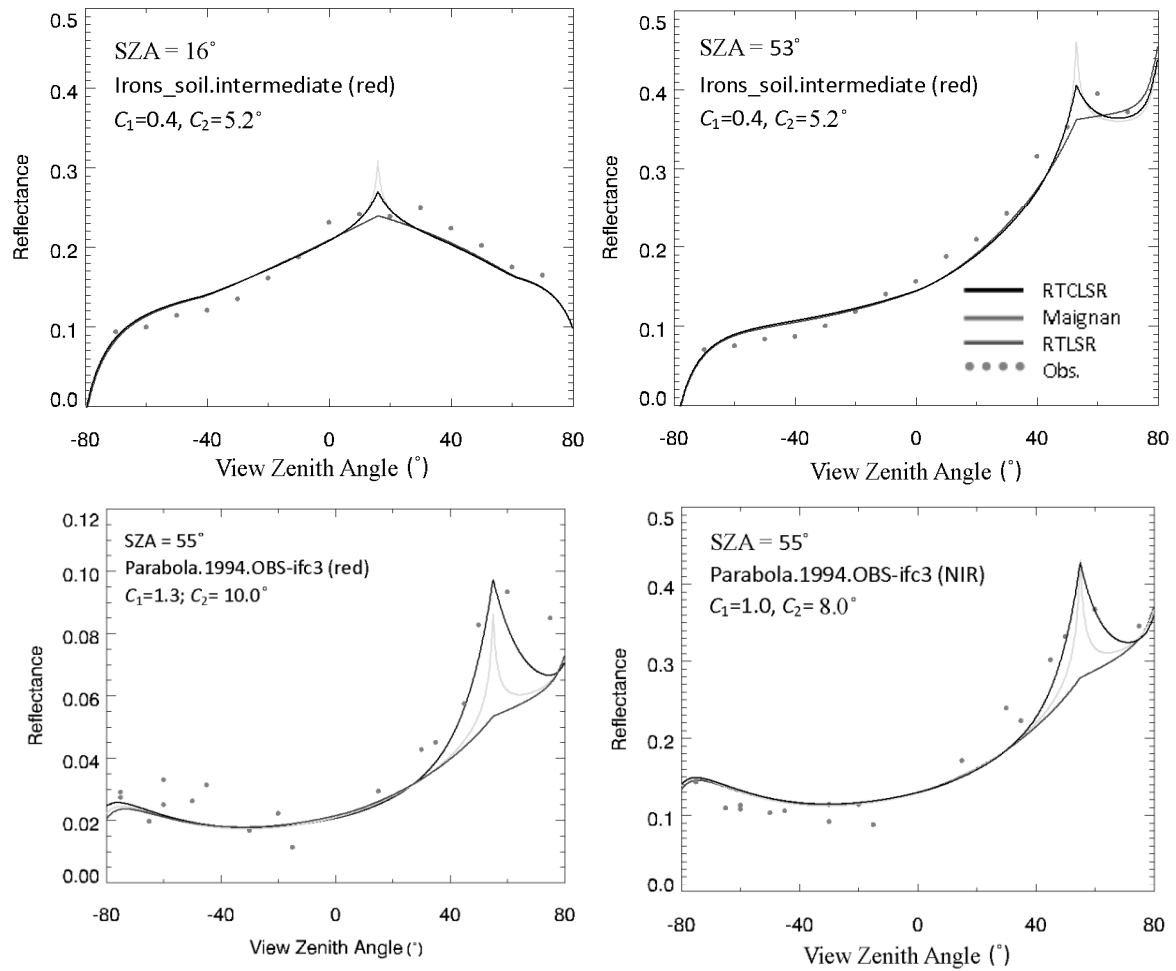1689 in the red band (a, b) and CAR Flight # 1693 in the NIR band (c, d)

788

789

790

791

792

793

794
795

Figure 10. Comparison of field soil measurements (top) and field old black spruce measurements

797 (bottom) with three models
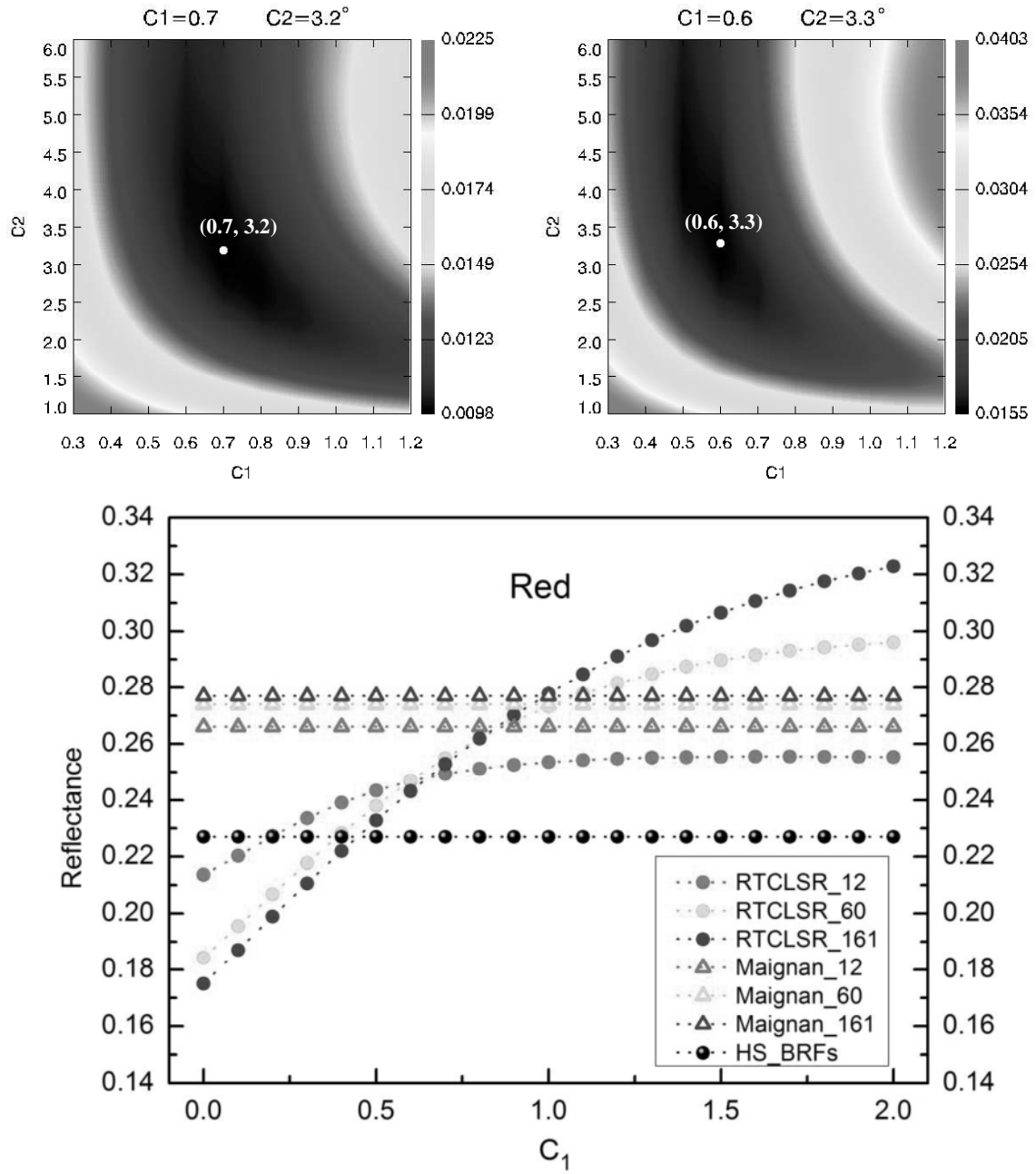
798

799

800

Figure 11. The fitting errors as functions of C_1 and C_2 for the entire POLDER data in the red (left) and in the NIR (right), and the white points on the contour plots represent the least fit-RMSEs with the optimal C_1 and C_2 values; the modeled hotspot reflectance as a function of C_1 (given $C_2 = 3°$) using CAR data to simulate three BRDF sample sizes (12, 60 and 161 samples) in the red band (bottom).
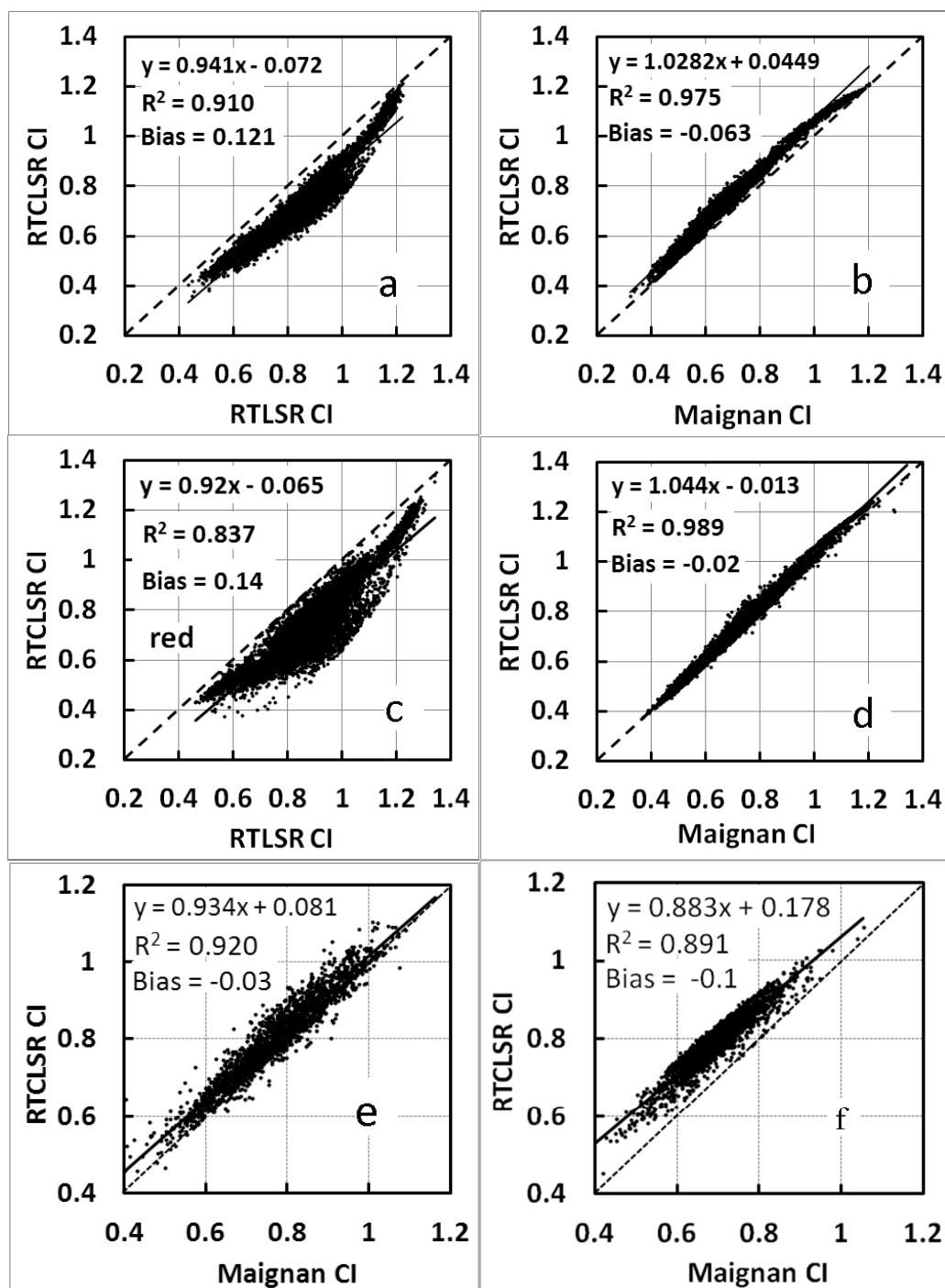
805

806

807

808

Figure 12. Comparison of CI retrievals between models using POLDER data in the NIR band (top) and in

the red band (middle), as well as using MODIS data (bottom) in the red and the in NIR bands. The dashed

and solid lines represent the one-to-one lines and the fitted lines, respectively.

812

References

Bicheron, P., & Leroy, M. (2000). Bidirectional reflectance distribution function signatures of major biomes observed from space. *J. Geophys. Res., 105*, 26669-26681.

Bacour, C. and Bréon, F.M. (2005) Variability of land Surface BRDFs. *Remote Sensing Environment*. 98, 80-95.

Bréon, F. M., Maignan, F., Leroy, M., & Grant, I. (2002). Analysis of hot spot directional signatures measured from space. Journal of Geophy-sical Research , 107(16), 4282 − 4296.

Bréon, F.M. and the Cnes PARASOL Team, PARASOL Level-1 Product Data Format and User Manual, Issue 1, Revision 1, May, 26th 2005 (www55).

Bréon, F. M., Fédèle, E.,Maignan, F., & Lacaze, R. (2007). A database of directional reflectance signature (GLC2000) with an analysis tool. *A-Train Symposium. Lille.*

Chen, J. M., Rich, P. M., Gower, S. T., Norman, J. M., & Plummer, S. (1997). Leaf area index of boreal forests: Theory, techniques, and measurements. Journal of Geophysical Research-Atmospheres, 102, 29429–29443.

Chen, J. M., Pavlic, G., Brown, L., Cihlar, J., Leblanc, S. G., White, H. P., et al. (2002). Validation of Canada-wide leaf area index maps using ground measurements and high and moderate resolution satellite imagery. *Remote Sensing of Environment*, 80, 165 − 184.

Chen, J.M., Menges, C.H., & Leblanc, S.G. (2005). Global mapping of foliage clumping index using multi-angular satellite data. *Remote Sensing of Environment, 97*, 447-457.

Chen, J. M., & Leblanc, S. G. (1997). A four-scale bidirectional reflectance model based on canopy architecture.*IEEE Transactions on Geoscience and Remote Sensing,* 35, 1316–1337.

Chen, J. M., & Cihlar, J. (1997). A hotspot function in a simple bidirectional reflectance model for satellite applications .*Journal of Geophysical Research-Atmospheres*, 102 , 25907 − 25913.

Chen, J. M., Rich, P. M., Gower, T. S., Norman, J. M., and Plummer, S. (1997), Leaf area index of boreal forests: theory, techniques and measurements. *J. Geophys. Res.* 102: 29,429–29,443.

Chopping, M., Moisen, G.G., Su, L.H., Laliberte, A., Rango, A., Martonchik, J.V., et al. (2008). Large area mapping of southwestern forest crown cover, canopy height, and biomass using the NASA Multiangle Imaging Spectro-Radiometer. *Remote Sensing of Environment, 112*, 2051-2063.

De Colstoun, B.E.C., & Walthall, C.L. (2006). Improving global scale land cover classifications with multi-directional POLDER data and a decision tree classifier. *Remote Sensing of Environment, 100*, 474-485.

Deering, D.W., Eck, T.F., & Banerjee, B. (1999). Characterization of the Reflectance Anisotropy of Three Boreal Forest Canopies in Spring–Summer. *Remote Sensing of Environment, 67*, 205-229.

Friedl, M.A., McIver, D.K., Hodges, J.C.F., Zhang, X.Y., Muchoney, D., Strahler, A.H., et al. (2002). Global land cover mapping from MODIS: algorithms and early results. *Remote Sensing of Environment, 83*, 168-182.

849   Friedl, M.A., Sulla-Menashe, D., Tan, B., Schneider, A., Ramankutty, N., Sibley, A., et al. (2010). MODIS
850   Collection 5 global land cover: Algorithm refinements and characterization of new datasets. *Remote*
851   *Sensing of Environment, 114*, 168-182.

852   Geiger, B., Franchistéguy, L., Carrer, D. andRoujean, J.-L. (2005). Land Surface Analysis Satellite
853   Application Facility (LSA-SAF) Product User Manual (PUM) on Albedo. Eumetsat, pp. 41.

854   Gatebe, C. K., King, M. D., Platnick, S., Arnold, G. T., Vermote, E. F., & Schmid, B. (2003). Airborne
855   spectral measurements of surface-atmosphere anisotropy for several surfaces and ecosystems over
856   southern Africa.Journal of Geophysical Research, 108 (D13).

857   Gatebe, C.K., Butler, J.J., Cooper, J.W., Kowalewski, M., & King, M.D. (2007). Characterization of
858   errors in the use of integrating-sphere systems in the calibration of scanning radiometers. *Applied*
859   *Optics*, 46, 7640-7651

860   Hautecoeur, O., & Leroy, M. M. (1998). Surface bidirectio nal refl ectance distribution function observed
861   at global scale by POLDER/ADEOS. *Geophysical Research Letters,* 25, 4197 − 4200.

862   Hill, M. J., Román, M. O., Schaaf, C. B., Hutley, L., Brannstrom, C., Etter, A., Hanan, N. P. (2011).
863   Characterizing vegetation cover in global savannas with an annual foliage clumping index derived
864   from the MODIS BRDF product, *Remote Sensing of Environment,* 115 (8): 2008-2024.

865   He, L., Chen, J. M., Pisek, J., Schaaf, C. B., Strahler, A. H. (2012). Global clumping index map derived
866   from the MODIS BRDF product, *Remote Sensing of Environment,* 119, 118-130.

867   Huang, X., Jiao, Z., Dong, Y., Zhang, H., & Li, X. (2013). Analysis of BRDF and Albedo Retrieved by
868   Kernel-Driven Models Using Field Measurements. *IEEE JOURNAL OF SELECTED TOPICS IN*
869   *APPLIED EARTH OBSERVATIONS AND REMOTE SENSING.* 6 (1): 149-161.

870   Irons, J.R., Campbell, G.S., Norman, J.M., Graham, D.W., & Kovalick, W.M. (1992). Prediction and
871   measurement of soil bidirectional reflectance. *Ieee Transactions on Geoscience and Remote Sensing,*
872   *30*, 249-260.

873   Jiao, Z., Woodcock, C., Schaaf, C.B., Tan, B., Liu, J., Gao, F., et al. (2011). Improving MODIS land cover
874   classification by combining MODIS spectral and angular signatures in a Canadian boreal forest.
875   *Canadian Journal of Remote Sensing, 37(2)*, 184-203.

876   Jiao, Z., & Li, X. (2012). Effects of multiple view angles on the classification of forward-modeled
877   MODIS reflectance. *Canadian Journal of Remote Sensing, 38 (4)*, 461-474.

878   Jiao, Z., Zhang, H, Li, X. (2012a). To derive a prior database of archetypal BRDF shapes from ground
879   measurements using anisotropic flat index (AFX). Geoscience and Remote Sensing Symposium
880   (IGARSS), 2012 IEEE International. 6753-6756, 22-27 July, Munich, Germany.

881   Jiao, Z., Hill, M., Schaaf, B. C., Zhang, H., Wang, Z. ,Li, X. (2014). An Anisotropic Flat Index (AFX) to
882   derive BRDF Archetypes from MODIS, *Remote Sensing of Environment*, 141: 168–187.

883   Jiao, Z., Zhang, H., Dong, Y., Liu, Q., Xiao, Q., Li, X. (2015). An algorithm for retrieval of surface albedo
884   from small view-angle airborne observations through the use of BRDF archetypes as prior
885   knowledge. IEEE JOURNAL OF SELECTED TOPICS IN APPLIED EARTH OBSERVATIONS

886   AND REMOTE SENSING, DOI: 10.1109/JSTARS.2015.2414925, accepted.

887 Justice, C.O., Román, M.O., Csiszar, I., Vermote, E., Wolfe, R., Hook, S.J., Friedl, M., Wang, Z., Schaaf, C.,
888   Miura, T., Tschudi, M., Riggs, G., Hall, D.K., Lyapustin, A., Devadiga, S., Davidson, C., & Masuoka, E.
889   (2013). Land and Cryosphere Products from Suomi NPP VIIRS: Overview and Status. *Journal of*
890   *Geophysical Research-Atmospheres, 118*, 1-13, doi:10.1002/jgrd.50771

891 Jupp, D. L., and A. H. Strahler, A hot spot model for leaf canopies, *Remote Sens. Environ.* , 38 , $193-210$,
892   1991.

893 King, M. D., Menzel, W. P., Grant, P. S., Myers, J. S., Arnold, G. T., Platnick, S. E., et al. (1996). Airborne
894   scanning spectrometer for remote sensing of cloud, aerosol, water vapor and surface properties.
895   *Journal of Atmospheric and Oceanic Technology*, 13, 777–794.

896 Kuusk, A. (1991). The hotspot effect in plant canopy reflectance, in Photon-Vegetation Interactions.
897   Applications in Optical Remote Sensing and Plant Ecology (R. B. Myneni and J. Ross, Eds.),
898   Springer-Verlag, Berlin,   pp. 139-159.

899 Li, X., Gao F, Wang J D and Strahler A H. (2001). A priori knowledge accumulation and its application to
900   linear BRDF model inversion. Journal of Geophysics Research, 106(D11): 11925-11935.

901 Li, X., & Strahler, A.H. (1992). Geometric-optical bidirectional reflectance modeling of the discrete
902   crown vegetation canopy: effect of crown shape and mutual shadowing. *Ieee Transactions on*
903   *Geoscience and Remote Sensing, 30*, 276-292.

904 Li, Z., Cihlar, J., Zheng, X., Moreau, L. and Ly, H. (1996). The bidirectional effects of AVHRR
905   measurements over boreal regions," IEEE Trans.Geosci. Remote Sens., 34, 1308–1322.

906 Litvinov, P, Hasekamp, O., Cairns, B. (2011). Models for surface reflection of radiance and polarized
907   radiance: Comparison with airborne multi-angle photopolarimetric measurements and implications
908   for modeling top-of-atmosphere measurements. *Remote Sensing of Environment*, 115, $781-792$.

909 Leroy, M., & Roujean, J.L. (1994). Sun and view angle corrections on reflectances derived from
910   NOAA/AVHRR data. *IEEE Transactions on Geoscience and Remote Sensing, 32*, 684-697.

911 Lucht W, Schaaf C B and Strahler A H. 2000. An algorithm for the retrieval of albedo from space using
912   semiempirical BRDF models. *IEEE Transactions on Geoscience and Remote Sensing,* 38(2):
913   977-998 .

914 Maignan, F., Bréon, F.M. and Lacaze, R. (2004). Bidirectional reflectance of Earth targets: evaluation of
915   analytical mode ls using a large set of sp aceborne measurements with emphasis with the hot spot,
916   Remote Sens. Environ., 90, 210-220.

917 Qin, W. & Goel, N. (1995). An evaluation of hotspot models for vegetation canopies, *Remote Sensing*
918   *Reviews*, 13 (1-2), 121-159.

919 Qin, W., and Jupp, D.L.B. (1993). An analytical and computationally efficient reflectance model for leaf
920   canopies, Agric. Meteorol., 66, 31-64.

921 Qin, W., and Xiang, Y. (1994). On the Hotspot Effect of Leaf Canopies: Modeling Study and Influence of
922   Leaf Shape. *Remote Sensing of Environment*, 50, $95-106$.

923 Roujean, J.-L., Leroy, M., & Deschamps, P.-Y. (1992). A Bidirectional Reflectance Model of the Earth's
924   Surface for the Correction of Remote Sensing Data. *J. Geophys. Res., 97*, 20455-20468.

925 Roujean, J.-L. (2000). A Parametric Hot Spot Model for Optical Remote Sensing Applications. *Remote*
926   *Sensing of Environment, 71*, 197-206.

927 Ross, J.K. (1981). *The Radiation Regime and Architecture of Plant Stands*. Norwell, MA: Dr. W. Junk,
928   392 pp.

929 Román, M. O., C. B. Schaaf, P. Lewis, F. Gao, G. P. Anderson, J. L. Privette, A. H. Strahler, C. E.
930   Woodcock, and M. Barnsley (2010), Assessing the coupling between surface albedo derived from
931   MODIS and the fraction of diffuse skylight over spatially-characterized landscapes, *Remote Sensing*
932   *of Environment*, *114*(4), 738-760, doi:10.1016/j.rse.2009.11.014.

933 Román, M. O., C. K. Gatebe, C. B. Schaaf, R. Poudyal, Z. Wang, King, M. D. (2011). Variability in
934   surface BRDF at different spatial scales (30 m - 500 m) ov er a mixed agricultural landscape as
935   retrieved from airborne and satellite spectral measurements, *Remote Sensing of Environment*, 115,
936   2184-2203, 2011.

937 Sellers, P. J., Los, S. O., & Tucker, C. J. (1994). A global 1- 1- NDVI data set for climate studies. Part 2:
938   The generation of global fields of terrestrial biophysical parameters from the NDVI. *International*
939   *Journal of Remote Sensing*, 11, 95–111.

940 Schaaf, C.B., Gao, F., Strahler, A.H., Lucht, W., Li, X., Tsang, T., et al. (2002). First operational BRDF,
941   albedo nadir reflectance products from MODIS. *Remote Sensing of Environment, 83*, 135-148.

942 Strugnell, N., W. Lucht, and Schaaf, C. (2001). A global albedo data set derived from AVHRR data for use
943   in climate simula tions, Geophys. Res. Let., 28, 191-194.

944 Shuai, Y., Schaaf, C.B., Strahler, A.H., Liu, J., & Jiao, Z. (2008). Quality assessment of BRDF/albedo
945   retrievals in MODIS operational system. *Geophysical Research Letters*, 35, L05407

946 Tsay, S.C., King, M.D., Arnold, G.T., & Li, J.Y. (1998). Airborne spectral measurements of surface
947   anisotropy during SCAR-B. *Journal of Geophysical Research-Atmospheres, 103*, 31943-31953.

948 Van Leeuwan, W. and Roujean, J.-L. (2002). Land surface albedo from the synergistic use of polar (EPS)
949   and geo-stationary (MSG) obser ving systems an assessment of physical uncertainties, *Remote Sens.*
950   *Environ.*, 81, no2-3, 273-289, 2002.

951 Wang, Z., Schaaf, C.B., Lewis, P., Knyazikhin, Y., Schull, M.A., Strahler, A.H., et al. (2011). Retrieval of
952   canopy height using moderate-resolution imaging spectroradiometer (MODIS) data. *Remote Sensing*
953   *of Environment, 115*, 1595-1601.

954 Wang, Y.,A. Lyapustin, J.L. Privette, R.B. Cook, S.K. SanthanaVannan, E.F.Vermote, Schaaf, C. (2010).
955   Assessment of biases in MODIS surface reflectance due to Lambertian approximation, *Remote*
956   *Sensing of Environment*, 114,2791-2801.

957 Wanner, W., Li, X., & Strahler, A.H. (1995). On the derivation of kernels for kernel-driven models of
958   bidirectional reflectance. *J. Geophys. Res., 100*, 21077-21089.

959 Zhu, G., Ju, W., Chen, J. M., Gong, P., Xing, B. and Zhu, J.(2012). Foliage Clumping Index Over China's

960   Landmass Retrieved From the MODIS BRDF Parameters Product, *IEEE Transactions on*
961   *Geoscience and Remote Sensing*, 50 (6), 2122-2137.
962   Zhang, X., M.A. Friedl, C.B. Schaaf, A. H. Strahler, J.C.F. Hodges, F. Gao, B. C. Reed, and A. Huete
963   (2003). Monitoring vegetation phenology using MODIS, *Remote Sensing of Environment,* 84,
964   471-475.
965